# Origin of Sr-enriched glassy picrites from the Karoo Large Igneous Province

**L. D. Ashwal[1], A. Ziegler[2], T. Truebody[1†] and R. Bolhar[1]**

[1]School of Geosciences, University of the Witwatersrand, Private Bag 3, WITS 2050, Johannesburg, South Africa

[2]Microscopy and Microanalysis Unit, University of the Witwatersrand, Private Bag 3, WITS 2050, Johannesburg, South Africa

Corresponding author: Lewis Ashwal (lewis.ashwal@wits.ac.za)

[†]Current address: Amatshe Mining, P.O. Box 36432, Hall Road, Menlo Park, Johannesburg 0102, South Africa

Key Points:

- Microbeam measurements of phases in six incompatible element rich Karoo picrites show that the glass phases represent the repositories for K, Sr, Ba and Zr.
- Glasses formed by fractional crystallization of olivine, pyroxene, ilmenite and apatite from enriched parental melts derived from the mantle lithosphere.
- The unusual compositions of the picrites and their calculated parental melts suggest a possible link to processes that gave rise to kimberlite magmatism.

## Abstract

Magmatic products of the Karoo Large Igneous Province can be divided into a volumetrically dominant, compositionally uniform low-Ti tholeiitic suite, and a subordinate, geographically restricted, compositionally diverse, incompatible-rich high-Ti suite. High-Ti picrites contain up to 2400 ppm Sr, 1900 ppm Ba and 550 ppm Zr, which seems unusual for olivine-enriched mafic rocks. We studied six Karoo picrites to determine the phase(s) in which Sr resides. Samples consist of 10–30% olivine phenocrysts in a groundmass of brown glass, augite, feldspar, ilmenite and apatite. Glass compositions vary, but are generally evolved, ranging from basaltic trachyandesite to trachyte to dacite. X-ray intensity maps demonstrate that most of the Sr resides in the glasses, and to a lesser extent, in feldspars, if present. The highest Sr (up to 9470 ppm) occurs in glasses adjacent to euhedral olivines, suggesting that phenocrysts are genetically related to evolved liquids represented by surrounding groundmasses. Compositional arrays formed by whole rocks (WRs) and bulk groundmasses represent liquid lines of descent. Calculated parental melts have much higher $K_2O$ and incompatible trace elements (e.g. Sr or Ba >1200 ppm) relative to low-Ti tholeiites. Fractional crystallization modelling yields evolved residual liquid compositions corresponding to those of glasses, and closely follow liquid evolution predicted by mass balance calculations involving mineral and bulk groundmass compositions. The unusual parental melt compositions imply derivation by small degrees of partial melting from SCLM mantle sources enriched in Sr and other incompatibles, and suggest a possible petrogenetic link between the high-Ti Karoo magmas and carbonatites and kimberlites.



## Plain Language Summary

Rocks rich in the mineral olivine should have compositions with only small amounts of elements that are unable to be accommodated in its crystal structure. In contrast, picrites from the Jurassic Karoo Large Igneous Province in southern Africa are extraordin**a**rily enriched in K, Sr, Ba, Zr and P, which is unusual. We used microbeam instruments to locate the repositories of these elements in six picrite samples, and found that they are highly concentrated in the glasses that formed as the magmas were quenched near the Earth's surface after having ascended from deeper levels. The glasses represent residual melts that formed by extensive earlier precipitation of olivine, pyroxene, ilmenite and apatite in a process called fractional crystallization. Elements that are generally excluded from these minerals became concentrated in the residual melts and eventually quenched to form glass. Our data allowed us to calculate original parental melt compositions for the picrites, and these have much higher K, Sr, Ba, Zr and other so-called "incompatible elements" relative to the vast majority of Karoo basaltic melts. This implies that the magmas parental to the picrites were derived by partial melting of a small region in the Earth's mantle that is unusually enriched in such elements, perhaps at depths of a few hundred kilometers. This implies a possible link between the Karoo picrites and kimberlites, which have similar chemical features and mantle sources.

## 1 Introduction

In his pioneering work on the Karoo region of southern Africa, Keith Cox recognized that the mafic magmatic rocks of continental flood basalt provinces, now associated with Large Igneous Provinces (LIPs), are divisible into two distinct geochemical types, one with unusual enrichments in K, Ti, P, Ba, Sr and Zr, and another with more "normal" tholeiitic compositions (Cox et al., 1965, 1967). This distinction, frequently designated as high- vs. low-Ti suites, has been corroborated for Karoo flows, sills and dikes by numerous subsequent studies (e.g. Duncan et al., 1984; Jourdan et al., 2007), and successfully applied to many other continental flood basalt provinces including the Deccan (Cox and Hawkesworth, 1985; Melluso et al., 2004), Paraná-Etendeka (Peate et al., 1992; Gibson et al., 1995), and Siberian Traps (Hawkesworth et al., 1995; Fedorenko et al., 1996) LIPs. The low-Ti suite is typically volumetrically predominant, and consists of compositionally uniform tholeiitic rocks, whereas the smaller volumes of high-Ti suite rocks are extraordinarily diverse, including basalts, picrites, andesites, nephelinites, lamproites and a variety of other unusual lithologies (Figure 1). The two suites commonly show geographic provinciality (Figure 2), a feature readily apparent for the Karoo LIP (Cox et al., 1967; Luttinen, 2017), as well as several other continental LIPs (Natali et al., 2017), but there is little consensus as to whether the geochemical differences reflect distinct mantle sources, degrees or depths of partial melting, and/or crustal contamination effects (e.g., Jourdan et al., 2007 and references therein). There is a substantial and growing literature on continental as well as oceanic LIPs, summarized in several books (Macdougall, 1988; Mahoney and Coffin, 1997; Ernst, 2014).

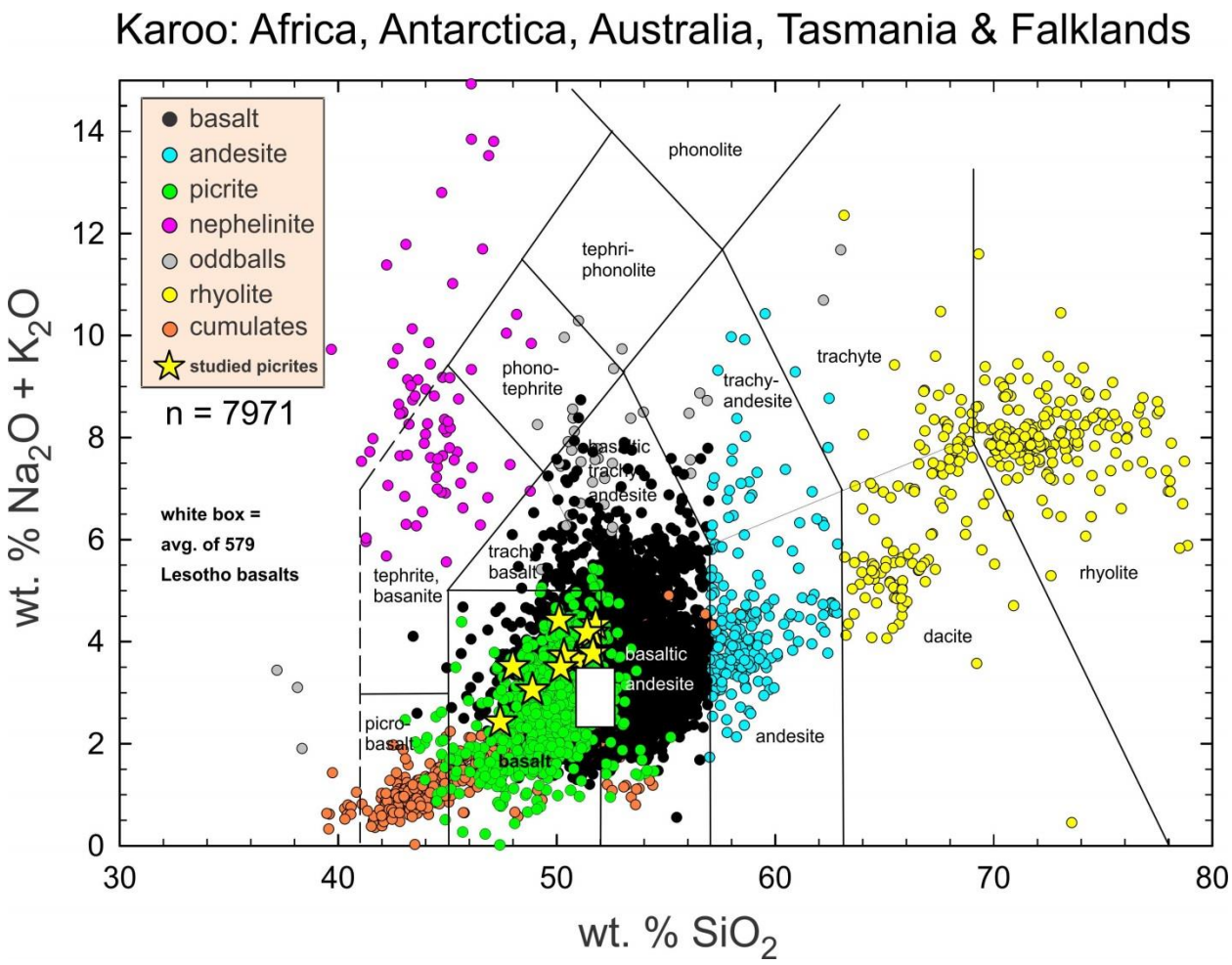


**Figure 1.** Total alkalies vs. silica (TAS) diagram showing compilation of 7971 whole rock major element analyses of Karoo magmatic rocks from South Africa, Lesotho, Eswatini (formerly Swaziland), Zimbabwe, Botswana, Mozambique, Namibia, Antarctica, Australia, Tasmania and the Falkland Islands. Data sources: Duncan et al. (1984) database (n = 4251), GEOROC database (n = 1868), published papers (n = 1575), unpublished data of J.S. Marsh (n = 277). The vast volumetric majority of Karoo mafic rocks are low-Ti tholeiites, which almost entirely plot inside the white box, representing the average of 579 Lesotho basalts. In contrast, the high-Ti rock suite is extremely compositionally variable, but has been over-sampled and over-analysed, out of proportion to its volume. Compositions of the six high-Ti alkali picrites studied in this paper (yellow stars) exceed the chemical variability of the low-Ti tholeiitic basalts. Karoo picritic rocks (green symbols), defined as having >12 wt. % MgO, are themselves compositionally variable, with $Na_2O + K_2O$ up to 5.4 wt. %. Note that a large number of basaltic rocks, defined as having $SiO_2$ = 45-57 wt. % and MgO <10 wt. % (black symbols), plot underneath the symbols for picrites, which are highlighted in this diagram. Samples designated as “oddballs” include shoshonites, nordmarkite and lamprophyre.

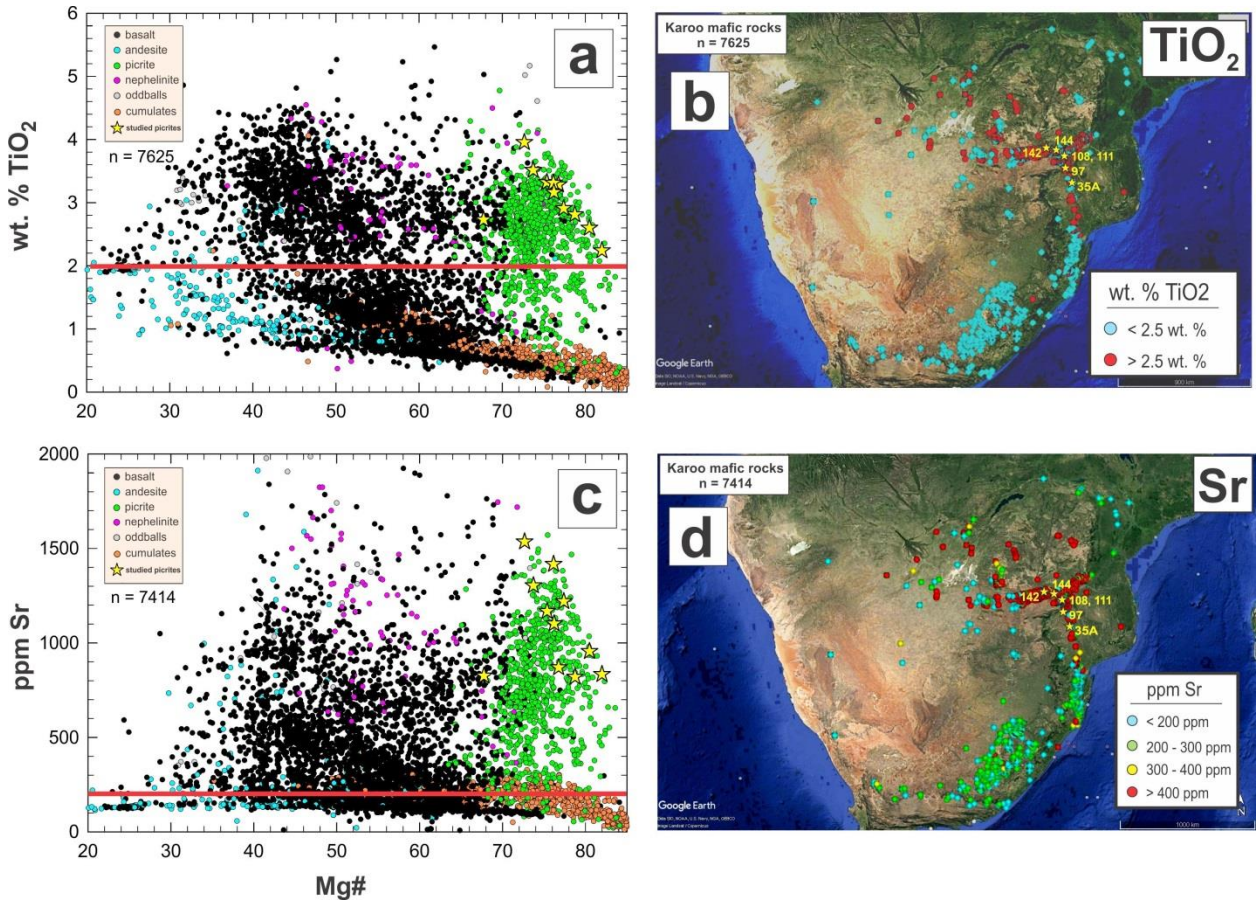


**Figure 2.** Left panel: Plots of Mg# vs wt. % $TiO_2$ (a) and ppm Sr (c) for Karoo mafic rocks (felsic rocks such as rhyolite and dacite are omitted). Compositions of the six alkali picrites studied in this paper are shown as yellow stars. Horizontal red lines separate the high-Ti and low-Ti rock suites, commonly chosen at $TiO_2$ = 2 wt.% and Sr = 200 ppm.
Right panel: Google Earth images of southern Africa showing locations of Karoo mafic rocks color-coded according to wt. % $TiO_2$ (b) and ppm Sr (d). Locations of our samples, with sample numbers are shown as yellow stars. High-Ti suite rocks are mainly concentrated in the arms of three intersecting dike swarms and linear belts of lavas in the Lebombo-Mwenezi, Sabi and Tuli regions.

We have compiled whole rock major, trace element and isotopic data for the Karoo LIP; the resulting database now includes nearly 8000 entries for occurrences in South Africa, Lesotho, Eswatini (formerly Swaziland), Zimbabwe, Botswana, Mozambique, Namibia, Antarctica, Australia, Tasmania and the Falkland Islands (Figure 1). An intriguing feature is that the high-Ti suite of Karoo mafic extrusive and intrusive rocks includes picrites (defined as having >12 wt. % MgO) with remarkable enrichments in large-ion lithophile elements (LILE): up to 1900 ppm Ba, 2400 ppm Sr, 550 ppm Zr, 3800 ppm P and 4.8 wt. % each of $K_2O$, and $TiO_2$ (Figure 2), which seems perplexing for such olivine-rich lithologies. In this paper, we report detailed mineralogical, geochemical and textural examination of six Karoo picrites, aimed at determining the phase(s) hosting the LILE, and the magmatic evolution and petrogenesis of these rocks.

## 2 Geological Setting

The Karoo LIP includes mafic to felsic magmatic rocks, variably exposed over an area of 2-3 x $10^6$ $km^2$, principally in southern Africa, but with correlatives in Antarctica (Ferrar Province), Australia and South America (Cox, 1988; Erlank, 1984 and papers therein; Marsh et al., 1997). The magmas were emplaced rapidly over a 2-3 m.y. period in the Early Jurassic (181 – 184 Ma) (Jourdan et al., 2008; Svensen et al., 2014), and have been widely linked to the impingement of a deep mantle plume into Precambrian continental lithosphere, which may have initiated the break-up of the Gondwana supercontinent (Storey, 1995; Storey and Kyle, 1997; Buiter and Torsvik, 2014). Magmatic products include erosional remnants of mainly basaltic lavas (reaching ~1.5 km thick in Lesotho) and networks of dikes and sill complexes, variably exposed over an area of at least 1 x $10^6$ $km^2$ in southern Africa and elsewhere (Figure 2). The LILE-enriched high-Ti suite of magmatic rocks is restricted mainly to the arms of three intersecting dike swarms and linear belts of lavas, interpreted as a triple junction, the center of which may represent the impingement site of the Karoo plume (e.g. Ernst and Buchan, 1997). Magma volumes are difficult to constrain with certainty because of extensive erosion and poor exposure, but can be estimated to be at least 2-3 x $10^6$ $km^3$, with the vast majority represented by low-Ti suite tholeiites (80-90%), and far lesser volumes (10-20%) of assorted high-Ti suite magmatic rocks.

The Karoo high-Ti picritic rocks, including the samples we studied, show enormous chemical variability relative to the extremely homogeneous, geographically widespread, low-Ti tholeiitic basalts as represented by the thick lava sequences in Lesotho (e.g. Marsh et al., 1997). This is illustrated in a TAS diagram (Figure 1), in which the picritic rocks (n = 897) show much larger ranges in $SiO_2$ and $Na_2O + K_2O$ than the Lesotho tholeiites (n = 579). The chemical variability of the picritic rocks relative to the tholeiites is demonstrated by their overall higher standard deviations of averages, which extends to all major and trace elements (Table 1). Picrites are enriched by factors of 2-4 relative to tholeiites in all incompatible trace elements, and even some compatible elements such as Cr, Co and Ni. The only exceptions are the HREE, which are 2-3 times higher in the tholeiites, owing to their flatter overall REE patterns (Table 1).

## 3 Sampling and Methodology

Thin section chips of six Karoo high-Ti suite picritic lavas, representing samples collected and studied by Bristow (1980, 1984), were provided by Prof. Chris Harris, University of Cape

Town. The picrites are all from the Letaba Formation in northern Lebombo – Mwenezi (formerly Nuanetsi) region, near the South Africa – Zimbabwe border (Figure 2). The Letaba Formation, dominated by picritic lavas, is up to 4 km thick, and is conformably underlain by nephelinites of the Mashkiri Formation (Cleverly and Bristow, 1979). GPS coordinates of our samples are given in Table 1, along with whole rock major and trace element chemical analyses from Bristow (1980) and Kamenetsky et al. (2017), who re-analyzed the same samples. Our samples show the following compositional ranges: MgO = 11.5 – 21.3 wt. %, $TiO_2$ = 2.6 – 4.0 wt. %, Sr = 826 – 1536 ppm, Ba = 667 – 1320 ppm and Zr = 302 – 587 ppm (Table 1). The chemical variability of these six samples exceeds that of the 579 Lesotho tholeiites constituting the dominant volume of Karoo magmas (Figure 1, Table 1). Standard polished thin sections were prepared and were used for all analytical data acquired in this study. Petrographically estimated modal abundances are given in Table 2.

Quantitative electron microprobe analyses of the major constituent phases- glasses, olivine, clinopyroxene, Cr-rich and Cr-poor spinel and ilmenite were obtained with an SXFive Field Emission EPMA instrument, equipped with 5 WDS spectrometers, and housed at the Microscopy and Microanalysis Unit (MMU), University of the Witwatersrand, Johannesburg. Operating conditions were: 15 kV accelerating potential, 20 nA beam current, <1μm spot diameter, and counting times of 20 and 10 s on peaks and backgrounds, respectively. For Cr-Fe-Ti oxide minerals, corrections were made for the overlap of the $TiK_\beta$ and $VK_\alpha$ X-ray peaks by subtracting a percentage of V counts determined empirically by measuring V on a V-free standard ($TiO_2$ or Ti metal). EPMA data are given in Table S1. Back-scattered electron (BSE) images and X-ray intensity maps were acquired using the same operating conditions as for quantitative elemental analyses. BSE images were obtained using 30 s frame times, and X-ray maps for individual elements were acquired using 750 – 1500 points, typically at 2 μm intervals, with dwell times of 10 ms per point.

Trace element concentrations of selected phases were acquired by LA-ICPMS at the Earthlab at the University of the Witwatersrand, employing an Australian Scientific Instruments (ASI) Resonetics Resolution 193 nm ArF excimer (SE 155) system coupled to a Thermo Scientific Fisher sector-field ICPMS (Element XR). Measurements were performed in low resolution and electrostatic scanning (E-scan) modes. Data were acquired by single spot analysis (diameter = 30-80 μm), using a laser repetition rate of 8 Hz and a fluence of 2.5 $Jcm^{-2}$. Total signal acquisition time was 65 sec to allow data processing and preparation for the next analysis, comprising 15 sec of pre- and post-ablation (gas blank) and 30 sec of ablation measurements. Laser sampling took place in a SE155 dual-volume ablation cell (Laurin Technic, Canberra, Australia) using a mixed He-Ar atmosphere and a small volume of $N_2$ to enhance signal stability and sensitivity. The following gas flows were applied: He (300-400 ml/min), Ar (800-1000 ml/min) and $N_2$ (3-5 ml/min), respectively. Synthetic glass NIST 612 (Jochum et al., 2011) served for calibration, while NIST 610 and 614 as well as USGS natural glasses BHVO2, BCR-2 and BIR-2 (Gao et al., 2002) were analysed as unknowns to evaluate accuracy and precision. The LA-ICPMS system was tuned during line scans using NIST 612 glass for maximum sensitivity for $^{6}Li$, $^{115}In$ and $^{238}U$, while maintaining oxide levels ($ThO^+/Th$) <0.5 %. For internal standardization, the isotopes $^{43}Ca$ or $^{29}Si$ were used. Typically, two analyses of the primary calibration standard were obtained at the beginning and end of an experiment, and 10-20 analyses of unknowns were followed by analyses of one primary calibration standard and two to

four analyses of the secondary standards for quality control purposes. Prior to each spot analysis surface material was removed using 2 laser pulses. The following masses were measured (6 samples per peak): $^{29}$Si, $^{43}$Ca, $^{45}$Sc, $^{47}$Ti, $^{51}$V, $^{53}$Cr, $^{59}$Co, $^{60}$Ni, $^{65}$Cu, $^{85}$Rb, $^{88}$Sr, $^{89}$Y, $^{90}$Zr, $^{93}$Nb, $^{139}$La, $^{140}$Ce, $^{141}$Pr, $^{146}$Nd, $^{147}$Sm, $^{151}$Eu, $^{157}$Gd, $^{159}$Tb, $^{163}$Dy, $^{165}$Ho, $^{166}$Er, $^{169}$Tm, $^{174}$Yb, $^{175}$Lu, $^{178}$Hf, $^{181}$Ta, $^{208}$Pb, $^{232}$Th, $^{238}$U. All isotopes were measured in triple mode, including pulse counting, analog and Faraday cup, depending on signal. Data reduction was performed using the iolite extension (http://www.iolite.org. au) to the software Igor Pro (http://www.wavemetrics.com), specifically the data reduction scheme ("DRS") "X_Trace_Elements_IS", proceeding in a series of sequential steps, including data import, selection of integrations, baseline subtraction, drift and down-hole fractionation, calibration and error propagation (Paton et al., 2010, 2011).

## 4 Results

### 4.1 Petrography

Petrographically estimated modal abundances of our samples are given in Table 2. Most consist of 10–30% euhedral to subhedral olivine phenocrysts and glomerocrysts (0.5 – 2 mm across), set in a fine-grained glassy groundmass (Figure 3); glass is absent in sample KP-144. Vesicles and amygdales are absent. Olivine phenocrysts in all samples contain 0.5 – 1% of small (10 – 300 μm), rounded, equant inclusions of Cr-rich spinel, and lesser amounts of partly crystallized, rounded melt inclusions (up to 100 μm across), similar to those described by Kamenetsky et al. (2017). The olivines have been variably serpentinized (5 – 18 %) along irregular fractures and phenocryst rims up to 250 μm across. One sample (KP-142) contains 4% of euhedral to subhedral clinopyroxene microphenocrysts up to 200 μm across, in addition to 16% olivine phenocrysts.

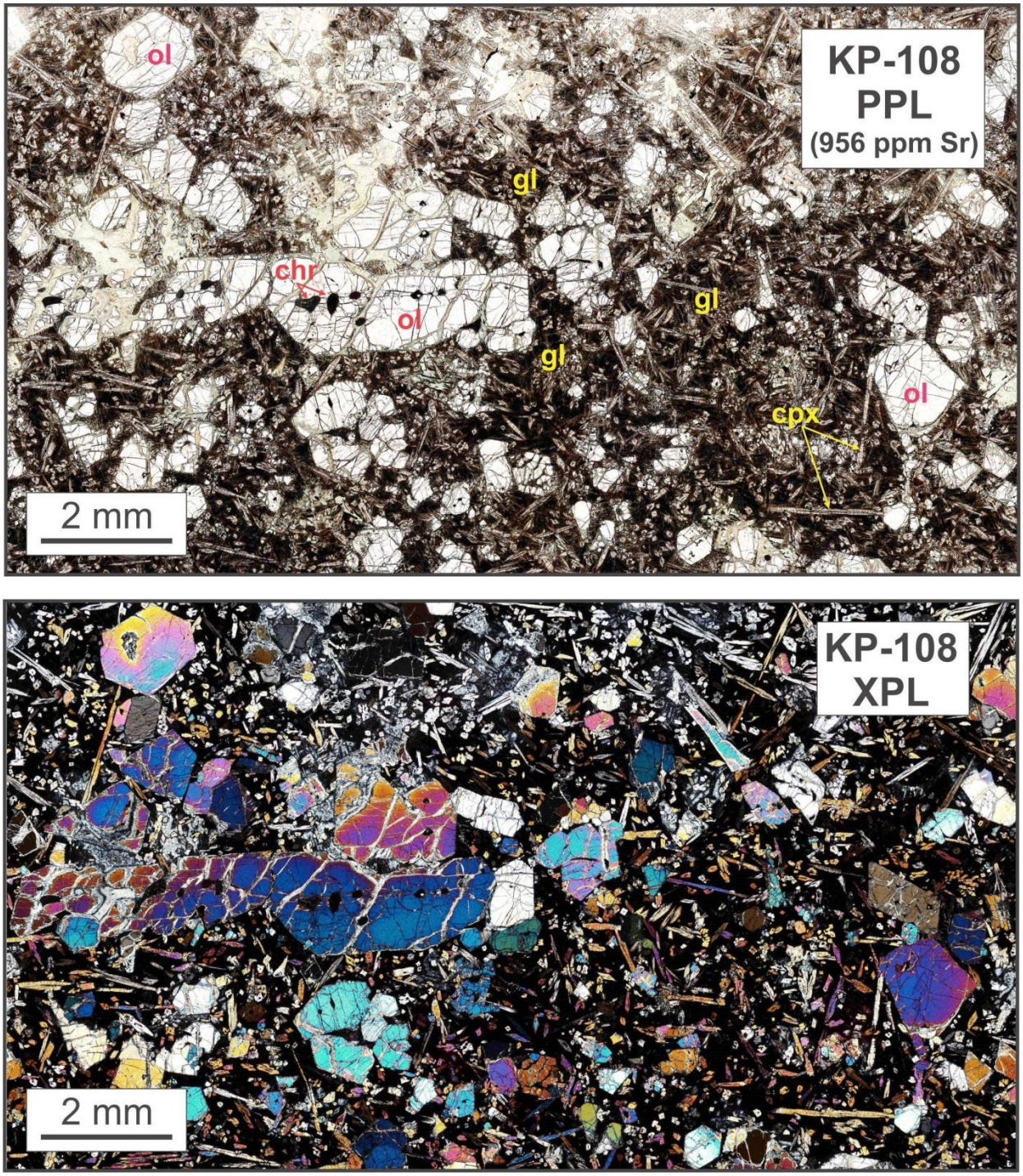


**Figure 3.** Full thin section photomicrographs of Sr-rich (956 ppm) picrite sample KP-108 in plane-polarized (top) and crossed-polarized (bottom) light, showing the textures and mineralogy typical of the samples studied in this paper. Olivine (ol) phenocrysts up to 2 mm across contain inclusions of Cr-rich spinel (chr), and the groundmass is composed of acicular clinopyroxene (cpx), dark brown glass (gl), ilmenite needles and apatite grains (both too small to be resolved at this scale).

The groundmass in most samples contains abundant (17 – 56%), irregular patches up to 4 mm across of unaltered, light to dark brown glass. Two samples, KP-97 and KP-111, have the unusual feature of containing two compositionally distinct glasses, which are distinguishable optically, in BSE images (Figure 4) and in X-ray maps. The dominant glass in the groundmass of these samples is lighter brown in color, has a lighter gray BSE response, and is designated as Type 1 glass. The darker brown glass, with darker gray BSE color, is lesser in volume, mainly occurs adjacent to olivine phenocrysts, and is designated as Type 2 glass. Boundaries between the two glasses are sharp, but irregular, as shown in BSE images (Figure 4). The principal groundmass minerals are clinopyroxene (20 – 40%), which occurs as irregular to acicular grains up to 400 μm long, ilmenite (4 – 10%) needles and skeletal grains up to 200 μm long, and equant grains of Fe-rich spinel (1 – 4 %) up to 100 μm across. Accessory apatite occurs as small equant grains and stubby needles up to 1 – 1.5 μm long. Two samples contain groundmass feldspars. Those in KS-35A (39% of groundmass) occur as subhedral laths up to 400 μm long, commonly with lamellar twinning; some grains show hollow, skeletal crystal forms. The laths are interstitial to larger clinopyroxene grains, and are closely associated with irregular patches of brown glass. Feldspars in KP-144 (49% of groundmass) occur as aggregates of untwinned, stubby laths up to 150 μm long, and irregular, anhedral grains. In some cases the laths form clusters of curved or bent crystals; less common are acicular needles up to 250 μm long. Patchy compositional zoning of KP-144 feldspars is evident in BSE images, which reveal irregular patches in the central regions of grains that have a darker BSE response, surrounded by brighter areas at the outer portions of grains. Orthopyroxene, while present in some Karoo picrites (Bristow, 1980, 1984), is absent in our samples, and secondary alteration products are completely absent in all groundmass phases.

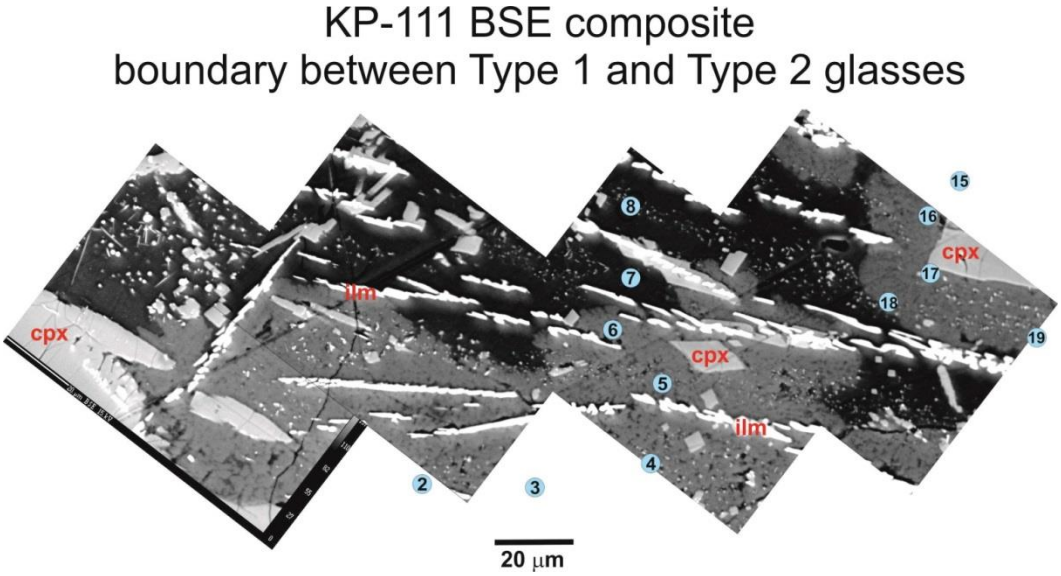


**Figure 4.** Composite BSE image of groundmass in sample KP-111 showing the sharp, but irregular boundary between Type 1 and Type 2 glasses. Type 2 glass (darker gray) has higher $Na_2O$, CaO and calculated $H_2O$, and lower $K_2O$, FeO, MgO and Mg# relative to Type 1 glass (lighter gray). Locations of EPMA analyses of glasses (Table S1) are shown as blue circles. Equant to irregular clinopyroxene (cpx) and needles of ilmenite (ilm) are labelled in red. Note the abundance of tiny mineral grains in both glasses, rendering spot analyses of pure glasses challenging.

## 4.2 Electron Microprobe Analyses

### 4.2.1 Olivine

Olivine phenocryst compositions are relatively homogeneous except for very thin rims (20 – 30 μm wide) that show continuous normal zoning to more Fe-rich compositions (Figure S3). Average core compositions range from $Fo_{82.02 \pm 1.1}$ in sample KP-144 to $Fo_{87.1 \pm 2.3}$ in sample KP-111 (Fo = molar Mg/[Mg+Fe]), with maximum variability of 3.6 mole % Fo (Figure 5, Table 2). Fe-rich rims range down to $Fo_{61.9}$ in sample KP-111, although serpentinization along phenocryst rims has variably obliterated the Fe-rich crystal edges; sample KP-142 has especially thick serpentine rims (up to ~250 μm) that have totally replaced the Fe-rich zoned phenocryst margins. Analyses of serpentine in KP-142 are given in Table S1. Ni and Cr concentrations in olivine correlate positively with Fo (cores up to 0.63 wt. % NiO, and 0.42 wt. % $Cr_2O_3$; rims down to 0.12 wt. % NiO, and 0.01 wt. % $Cr_2O_3$). Mn and Ti correlate negatively with Fo (cores down to 0.08 wt. % MnO, and 0.01 wt. % $TiO_2$; rims up to 0.51 wt. % MnO, and 0.12 wt. % $TiO_2$). We do not see the correlations between Fo and Ca that were reported in Karoo picritic olivines by Kamenetsky et al. (2017); CaO in the olivines we analyzed ranges from 0.15 – 0.41 wt. % CaO. Likewise, no correlations are apparent between Fo, and Al, Zn, Na or K.

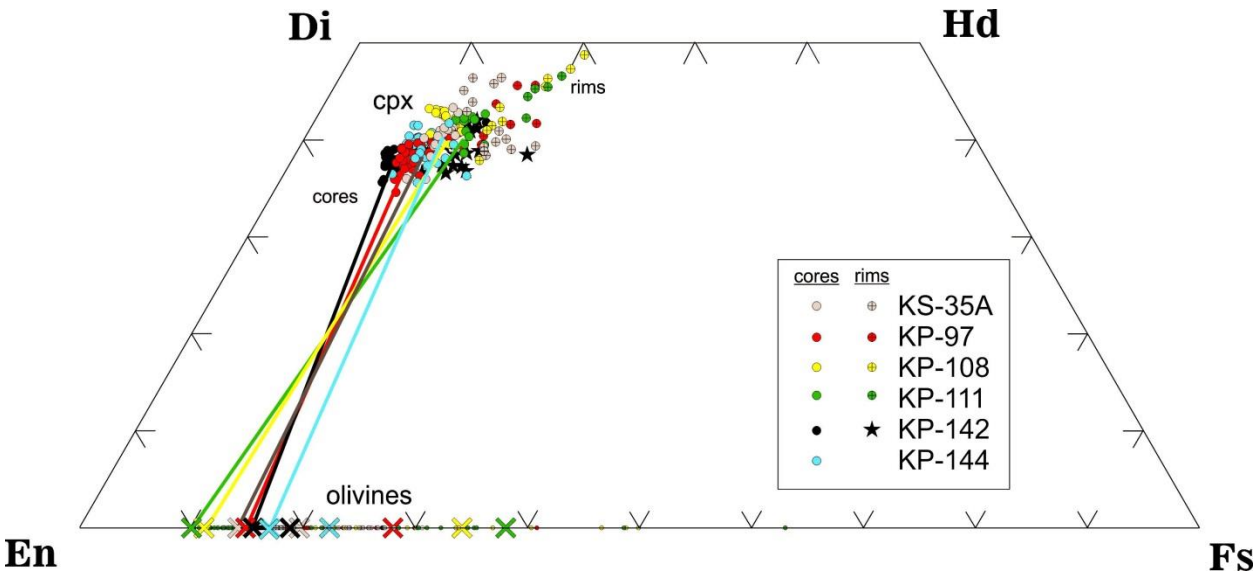


**Figure 5.** Pyroxene quadrilateral diagram showing compositions of clinopyroxenes and olivines in the studied picrite samples (Table S1). For clinopyroxenes, compositions of cores and rims are distinguished by different symbols. Minimum and maximum Fo contents of olivine phenocrysts are indicated by crosses. Tie lines connect mean clinopyroxene cores with maximum Fo content of coexisting olivine phenocrysts.

### 4.2.2 Clinopyroxene

All clinopyroxenes are compositionally zoned, showing Mg-rich and Ca-poor cores that vary continuously to more Fe- and Ca-rich regions toward grain edges (Figure 5, Table S1). The most primitive clinopyroxenes are the microphenocrysts in KP-142, which have cores of $Wo_{35.6-38.6}$, $En_{55.2-53.6}$, zoned to rims of Wo $_{41.8}$, $En_{42.8}$. Pyroxenes occurring as equant to acicular groundmass phases tend to be slightly less primitive, and have more fractionated grain edges, up to $Wo_{47.9-48.7}$, $En_{28.4-30.5}$ (Figure 5). Compositional profiles show strong positive correlations of Mg# (= molar Mg/[Mg+Fe]) with $Cr_2O_3$ and NiO, and negative correlations with $Al_2O_3$, $TiO_2$, MnO, $Na_2O$ and $K_2O$, such that the Mg-rich cores of phenocrysts and grains have low $Al_2O_3$ (~1 wt. %, Figure S1a), $TiO_2$ (~1 wt.%), MnO (~0.1 – 0.15 wt.%), $Na_2O$ (0.2 – 0.25 wt. %) and $K_2O$ (<0.05 wt. %), and high $Cr_2O_3$ (0.9 – 1.0 wt.%, Figure S1b) and NiO (0.12 wt. %). Grain edges and rims have very high $Al_2O_3$ (to 7 – 8 wt.%) and $TiO_2$ (to 4.2 – 4.9 wt. %), moderately high MnO (to 0.3 wt. %), $Na_2O$ (to 0.6 – 0.7 wt. %) and $K_2O$ (to 0.2 wt. %), and low $Cr_2O_3$ (<0.02 wt. %,) and NiO (<0.01 wt. %).

### 4.2.3 Spinels

The highly variable compositions of spinels (Figure 6, Table S1) correlate with their textural associations. Grains entirely enclosed within olivine phenocrysts have higher $Cr_2O_3$ and MgO relative to those at phenocryst edges or within the groundmass, which are enriched in $TiO_2$, FeO and $Fe_2O_3$. Overall, the spinel compositions form a trend from early Cr- and Mg-rich chromites towards Ti-rich magnetites that corresponds to the "Fe-Ti trend" of Barnes and Roeder (2001), and the "spinel gap" they describe is evident in our dataset. These features are illustrated in a triangular plot of molar $Fe^{3+}$-Cr-Al (Figure 6). The most evolved spinels are Ti-rich magnetites with $TiO_2$ = 11.3 – 19.5 wt.% that occur as equant groundmass phases in sample KP-111. In sample KP-144, spinel grains that protrude into the groundmass from within olivine phenocrysts show continuous zoning from Cr-rich interiors toward Fe- and Ti-rich compositions in the outer regions, as illustrated in X-ray element maps (Figure 7). Similar features were described by Barnes and Kunilov (2000) for picrites from the Noril'sk 1 and Talnakh intrusions of Siberia and by Scowen et al. (1991) for porphyritic olivine basalts in the Kilauea Iki lava lake, Hawaii, and were interpreted as reflecting reaction of Cr-rich spinels with evolving, trapped residual liquids.

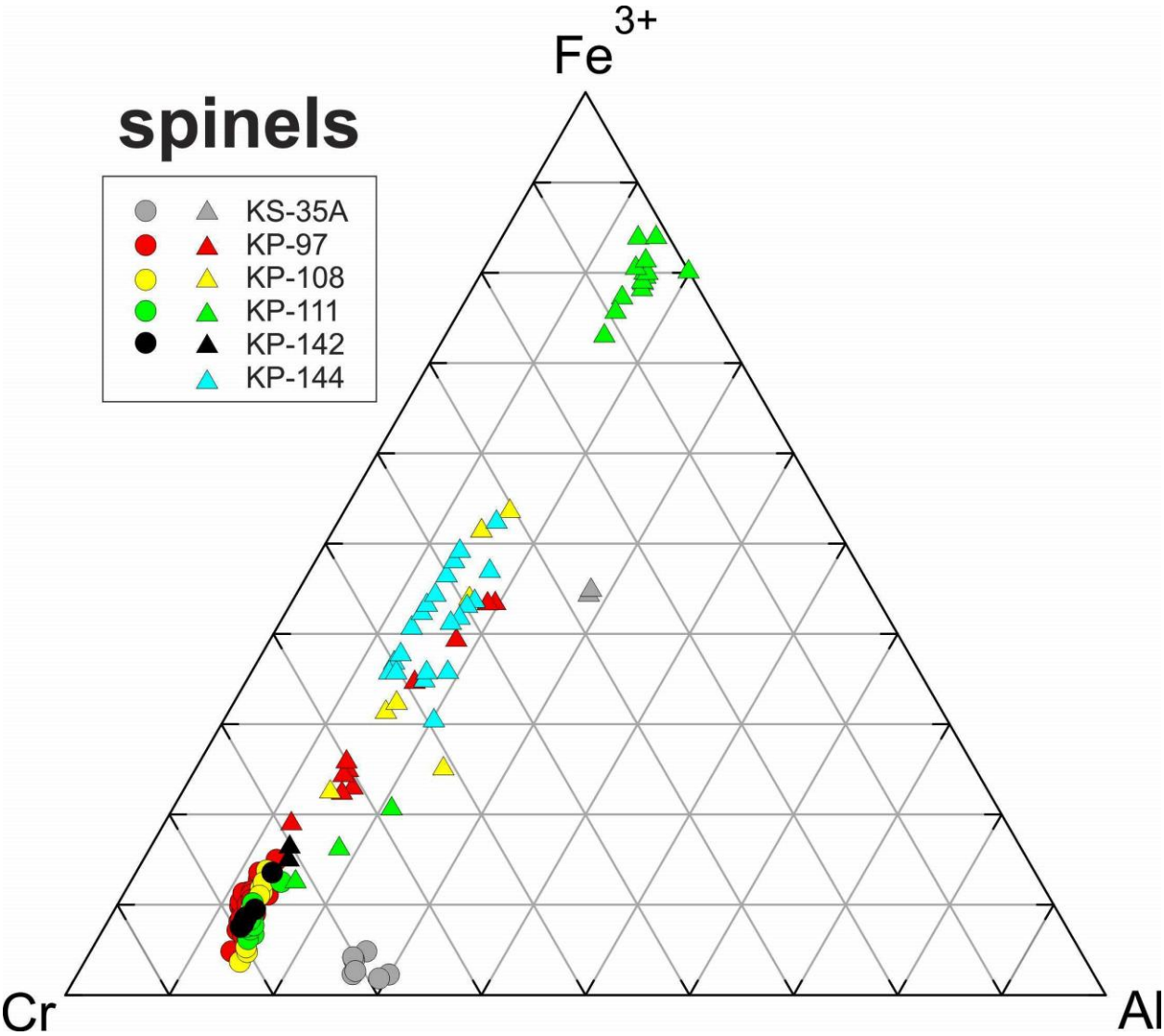


**Figure 6.** Triangular diagram of trivalent cations in spinels, calculated assuming ideal stoichiometry (Table S1). Early, Cr-rich spinels (circles) occur as inclusions in olivine phenocrysts. Matrix spinels (triangles) trend toward Ti-rich magnetites, occurring most prominently in sample KP-111. The overall array corresponds to the "Fe-Ti trend" of Barnes and Roeder (2001), and their "spinel gap" is evident between the matrix compositions and the Ti-rich magnetites in KP-111.

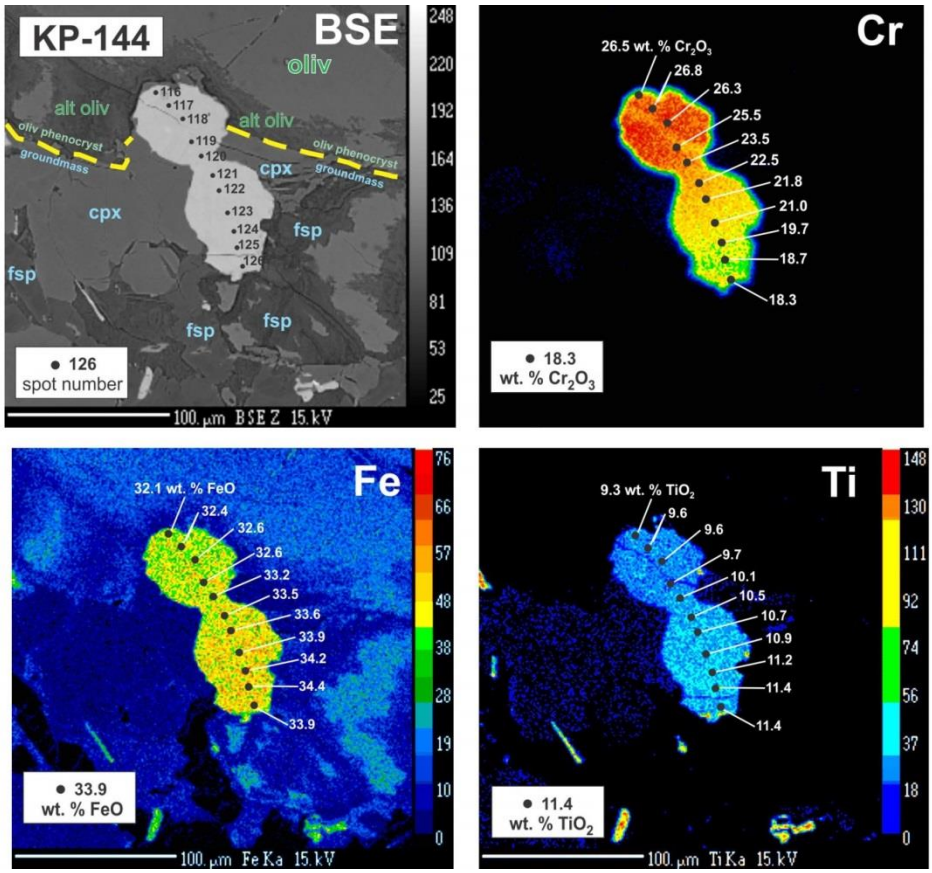


**Figure 7.** BSE and X-ray maps of a spinel grain protruding from within an olivine phenocryst into the groundmass. In the BSE image at top left, it can be seen that the rim of the olivine phenocryst has been altered to serpentine, but the original grain boundary is shown by a yellow dashed line. EPMA spot numbers refer to analyses given in Table S1. The spinel grain is continuously zoned from a Cr-rich interior toward outer regions enriched in Fe and Ti. Compositions determined by EPMA are expressed as wt. % $Cr_2O_3$, FeO and $TiO_2$ in the X-ray maps.

### 4.2.4 Ilmenite

Ilmenite needles in picrite groundmasses vary in composition, most notably in $TiO_2$ and MgO, which correlate positively from $TiO_2$ ~42 wt. % and MgO ~0.6 wt. % to $TiO_2$ ~51 wt. % and MgO ~5 wt.% (Figure 8, Table S1). There is also a weak correlation of $TiO_2$ with $Cr_2O_3$, but other elements show no significant correlations. The highest MgO and $TiO_2$ ilmenites in samples KP-97 and KP-144 approach the compositions of picroilmenites commonly found in kimberlites (Wyatt et al., 2004). Similar results for ilmenites in Karoo picritic rocks were reported by Cawthorn et al. (1989).

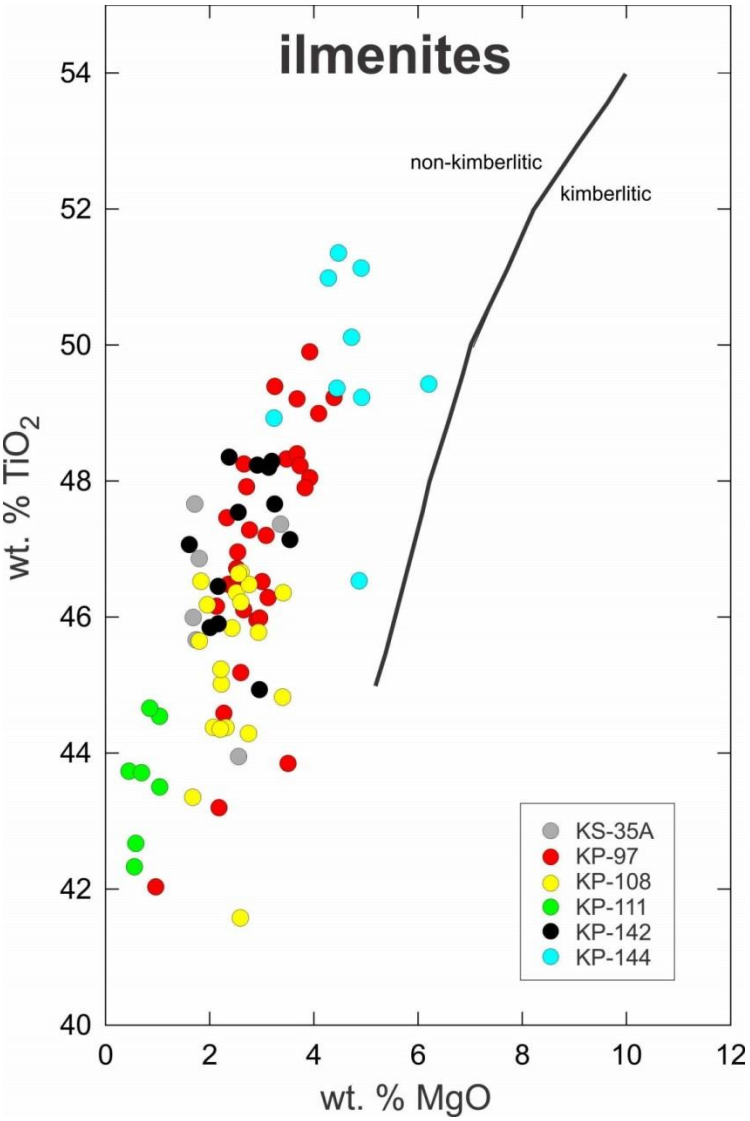


**Figure 8.** Plot of wt. % $TiO_2$ vs. MgO showing compositions of groundmass ilmenite needles (Table S1). The boundary between kimberlitic and non-kimberlitic ilmenite is from Wyatt et al. (2004).

### 4.2.5 Feldspars

Feldspar compositions in KS-35A and KP-144 (Table S1) are shown on an Ab-An-Or diagram in Figure 9. Subhedral feldspars in KS-35A are plagioclases that show an overall range from about $An_{51\text{-}52}Or_{3\text{-}5}$ to $An_{23\text{-}25}Or_{8\text{-}15}$ (average = $An_{42.2 \pm 8.2}Or_{5.9 \pm 3.1}$). Individual laths show restricted compositions that typically vary by less than 3-4 mole % An and Or; compositional zoning features are very minor to absent. In KP-144, the irregular, more centrally located patches with darker BSE response are enriched in plagioclase components, forming a cluster that ranges in composition from about $An_{15\text{-}19}Or_{21\text{-}23}$ to $An_{34\text{-}35}Or_{4\text{-}12}$. The outer regions of grains, with lighter BSE response, form a K-rich compositional array from about $An_{11\text{-}12}Or_{37\text{-}39}$ to $An_{2\text{-}3}Or_{80\text{-}81}$. There is a slight tendency for the most Or-rich compositions to occur near the outer rims of grains, but no systematic compositional zoning patterns are apparent. Feldspars from both samples have average $TiO_2 = 0.18 \pm 0.09$ wt. % and FeO = 0.81 ± 0.43 wt. % (n = 85) (Table S1). Feldspars and glasses in samples KS-35A and KP-144 plot between the 800°C and 1000°C solvus isotherms of Elkins and Grove (1990).

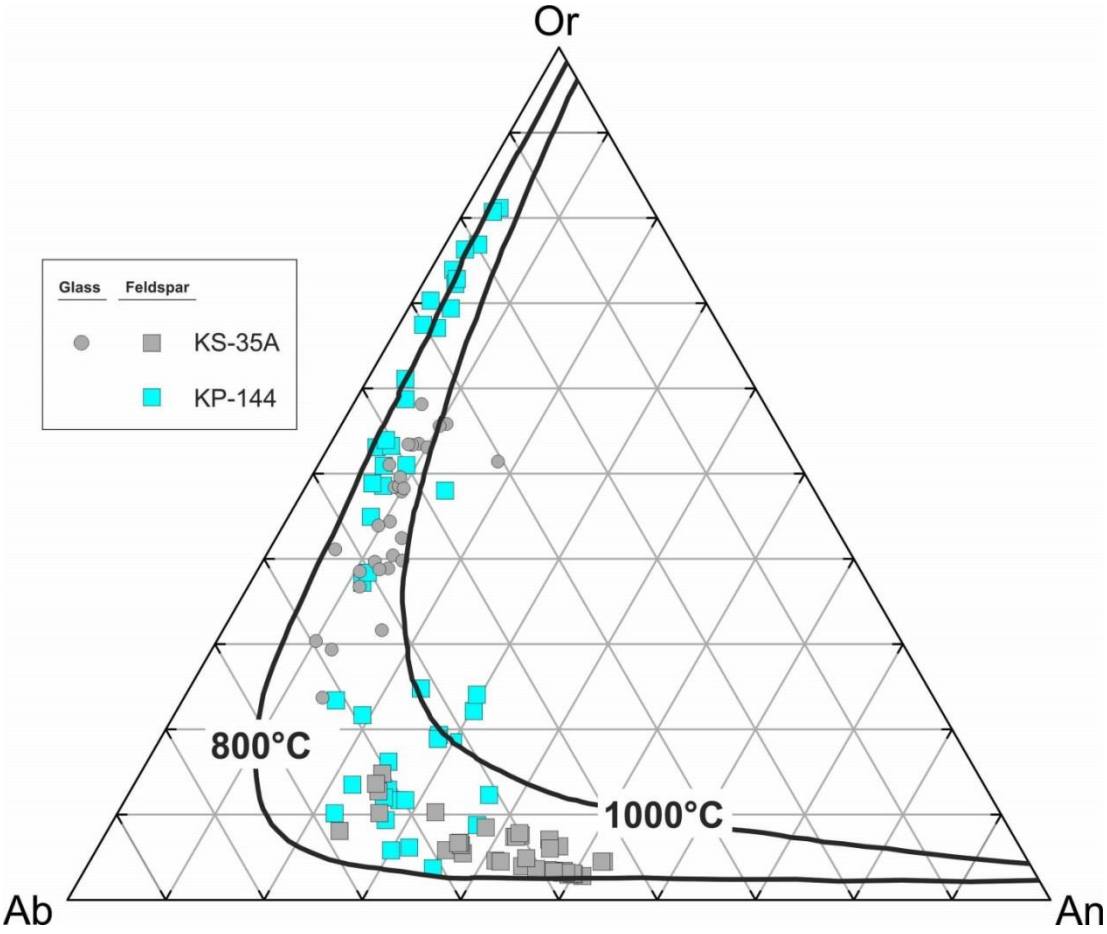


**Figure 9.** Ab-An-Or diagram showing compositions of feldspars (squares) in samples KS-35A and KP-144, and glasses (circles) in sample KS-35A (Table S1). Glasses plotted represent calculated normative compositions. Solvus isotherms are from Elkins and Grove (1990).

### 4.2.6 Glasses

Microprobe analyses of glasses are not straightforward because they contain variable amounts of tiny mineral inclusions (mainly clinopyroxene, ilmenite and apatite), which are not always visible optically or even in high-resolution BSE images. However, it is possible to recognize the chemical effects of incorporated mineral inclusions in individual spot analyses by abnormally high concentrations of MgO and CaO (for clinopyroxene inclusions), $TiO_2$ and FeO (for ilmenite) or $P_2O_5$ and CaO (for apatite), and in some cases the presence of multiple mineral inclusions can be identified in a similar way. A tabulation of individual glass analyses and averages that exclude (or minimize) mineral inclusions that were inadvertently (n = 307) is given in Table S1; spot analyses representing various mixtures of glass, clinopyroxene and ilmenite and/or apatite inclusions (n = 73) are highlighted and are excluded from the averages.

Most glasses are very rich in alkalies (~2 – 13 wt. % $Na_2O + K_2O$), and two compositional groups can be distinguished on a TAS diagram (Figure 10a). One group, with $Na_2O + K_2O$ = 6.3 – 13.2 wt. % and $SiO_2$ = 50 – 67 wt. %, includes glasses from KS-35A, KP-142, and Type 1 glasses in KP-97 and KP-111, and ranges in composition from basaltic trachyandesite to trachyte. A second group, including glasses from KP-108 and Type 2 glasses in KP-97 and KP-111, has $Na_2O + K_2O$ = 1.9 – 6.4 wt. % and $SiO_2$ = 55 – 68 wt. %, and ranges from andesite to dacite (Figure 10a). These groupings are maintained for some elements (Figure S2), but glasses from individual samples form distinct fields that overlap to varying degrees. Sample KP-142 contains the most compositionally variable glasses; those from some other samples form variably diffuse linear arrays on oxide-oxide plots (Figure S2). There is almost complete compositional overlap of fields for some elements like CaO, $P_2O_5$. The best chemical discriminators for the various types of glasses are the alkalies; fields for $SiO_2$ vs $Na_2O$ or $K_2O$ show the most distinct separation (Figure S2). Additional plots of glass compositions are given in Figures S4 – S 9.

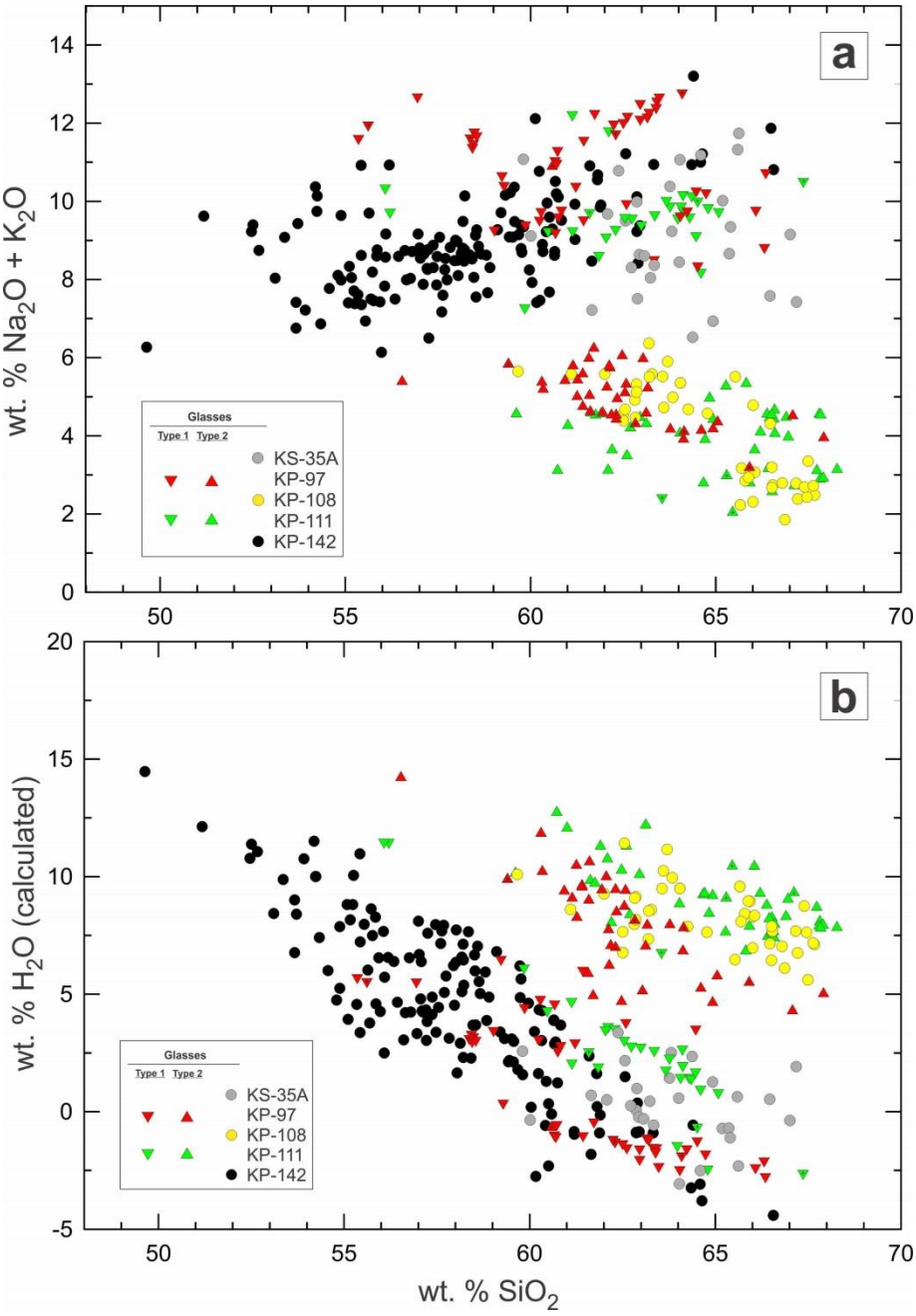


**Figure 10. (a)** Total alkalies – silica (TAS) diagram showing compositions of glasses in the studied picrite samples, as determined by EPMA. Two groupings are apparent, with one group having higher $Na_2O + K_2O$ (includes glasses in samples KS-35A, KP-142 and Type 1 glasses in KP-97 and KP-111) and a second group with lower $Na_2O + K_2O$ (includes glasses in from KP-108 and Type 2 glasses in KP-97 and KP-111). Spot analyses clearly representing mixtures of glasses with incorporated mineral inclusions are omitted.
**(b)** Plot of wt.% $SiO_2$ vs wt. % $H_2O$ (calculated as difference from EPMA summation totals) for glasses in the studied picrite samples.

For samples KP-97 and KP-111, Type 1 glasses, the dominant groundmass phase, have markedly higher $K_2O$ (8.2 – 12.6 wt. %) and lower $Na_2O$ (0.13 – 0.45 wt. %) relative to Type 2 glasses ($K_2O$ = 2.1 – 4.7, $Na_2O$ = 1.8 – 2.9 wt. %), which occur adjacent to olivine phenocrysts. This is readily apparent in X-ray maps for K and Na (Figure S3). Type 1 glasses are also relatively enriched in MgO, FeO and MnO, depleted in $TiO_2$ and CaO, but show almost complete overlap for $Al_2O_3$ and $P_2O_5$.

EPMA summation totals for glasses are remarkably variable between and within different samples, indicating the variable presence of volatile components, probably mainly or entirely $H_2O$; this is currently being tested with SIMS spot analyses. Glasses in KP-108 and Type 2 glasses in KP-97 and KP-111 have average totals of ~91-92 wt. %, implying as much as 8 – 9 wt. % volatiles, whereas those in KS-35A, and Type 1 glasses in KP-97 and KP-111 have totals approaching 100%, suggesting that volatiles are far less abundant or possibly absent (Figure 10b). Overall, the $H_2O$ contents of glasses as calculated by difference from summation totals show similar groupings to those evident for $SiO_2$ vs. $Na_2O + K_2O$ (Figure 10). Glasses in KP-142 have calculated $H_2O$ contents up to ~15 wt. % and show a negative correlation with $SiO_2$ content (Figure 10b).

### 4.3 X-ray maps and BSE Images

We obtained BSE images and X-ray element maps of our Karoo picrite samples in order to identify the repository phase(s) for the high incompatible trace element concentrations revealed by the whole rock data. Viable possibilities include glasses, feldspars, apatite, secondary alteration products like serpentine, and possibly clinopyroxene. We chose to investigate the distribution of Sr as an indicator of incompatible trace element enrichment. Figure 11 shows a BSE image and X-ray maps for P, Ti and Sr in sample KP-144, which contains 20% olivine phenocrysts and a groundmass consisting of 49% feldspar, 40% clinopyroxene, 10% ilmenite and 1% apatite; glass is absent from this sample (Table 2). The X-ray map for P (Figure 11b) shows that apatite occurs as equant and elongate grains up to 20 μm across and ilmenite occurs as abundant needles and blocky grains up to 500 μm across, as shown by the Ti X-ray map (Figure 11c). The X-ray map for Sr (Figure 11d) reveals that apatite, ilmenite, olivine and serpentinized olivine are virtually devoid of Sr, and that clinopyroxene may contain minor Sr concentrations. Rather, the main repository for Sr in this sample appears to be the groundmass feldspar. Note that the high apparent X-ray response for Sr in Cr-rich spinel is caused by an overlap of the Sr $L_\alpha$ X-ray peak (used for imaging) with a 3$^{rd}$-order Cr $K_\alpha$ peak, and reflects Cr, rather than Sr concentration (Figures 11d, 12b, S3).

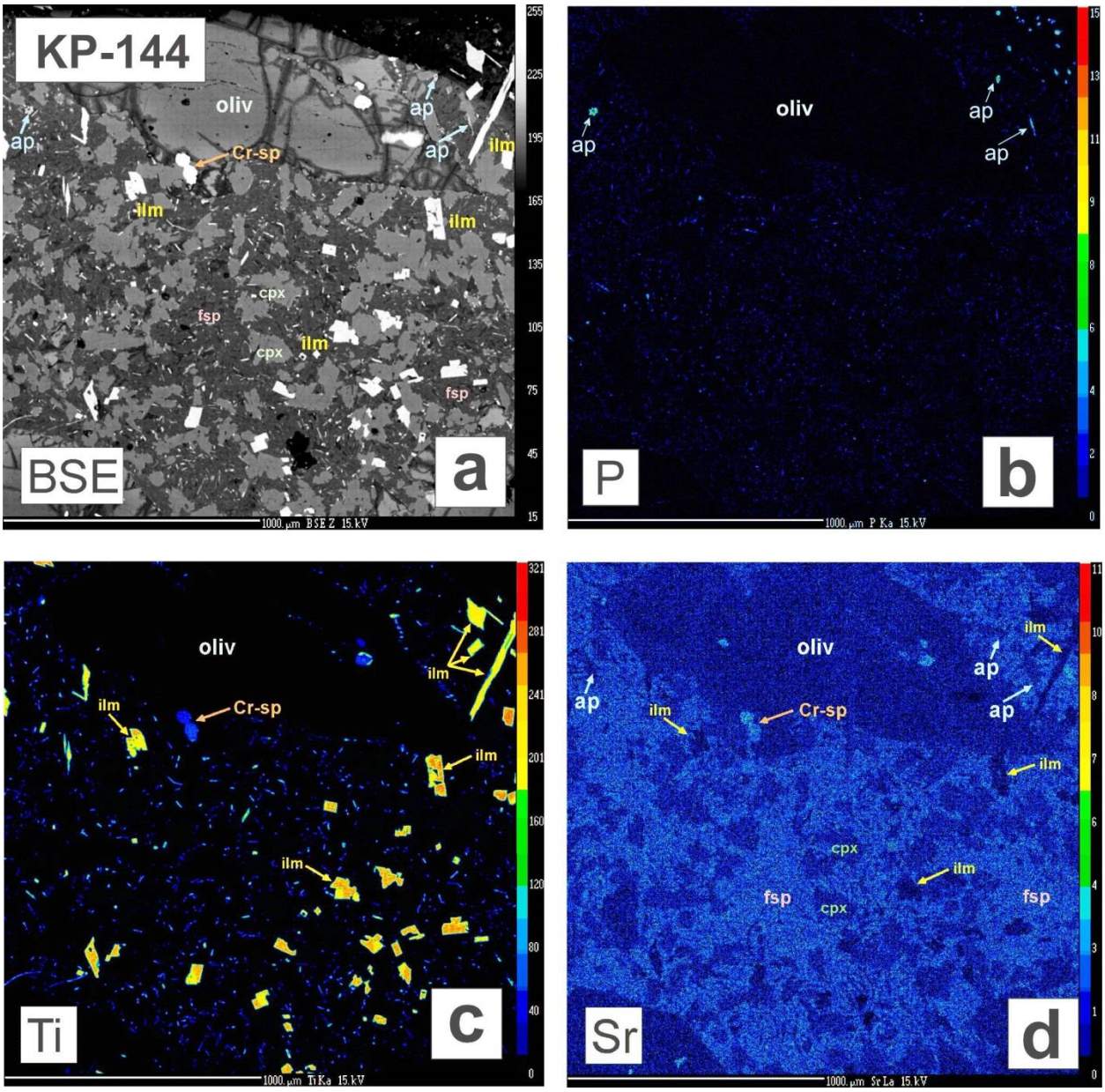


**Figure 11.** Back-scattered electron (BSE) image (a) for a part of picrite sample KP-144 and X-ray maps for P (b), Ti (c) and Sr (d). This sample contains 20% olivine phenocrysts and a groundmass with 49% feldspar, 40% clinopyroxene, 10% ilmenite needles and 1% apatite. Glass is absent. The X-ray image at bottom right shows that Sr is concentrated in feldspar, and to a far lesser extent, in clinopyroxene, but is absent from all other phases. Note that the high counts for Sr in Cr-rich spinel are caused by an overlap between the Sr $L_\alpha$ X-ray peak (which was used for imaging) with a 3$^{rd}$-order Cr $K_\alpha$ peak, and reflects Cr, rather than Sr concentration.

Images for sample KP-97 (30% olivine phenocrysts, groundmass composed of 63% Type 1 and Type 2 glasses, 30% clinopyroxene, 6% ilmenite and 1% apatite) are shown in Figure 13. The X-ray map for Sr (Figure 12b) clearly shows that the glasses are the main repository of Sr, with Type 2 glass, which occurs adjacent to olivine phenocrysts, having much higher concentrations relative to Type 1 glass, which is the dominant phase in the groundmass of this sample. Clinopyroxene grains in the groundmass show modest X-ray signals for Sr. Quantification of the trace element concentrations of glasses and other phases is discussed in the next section.

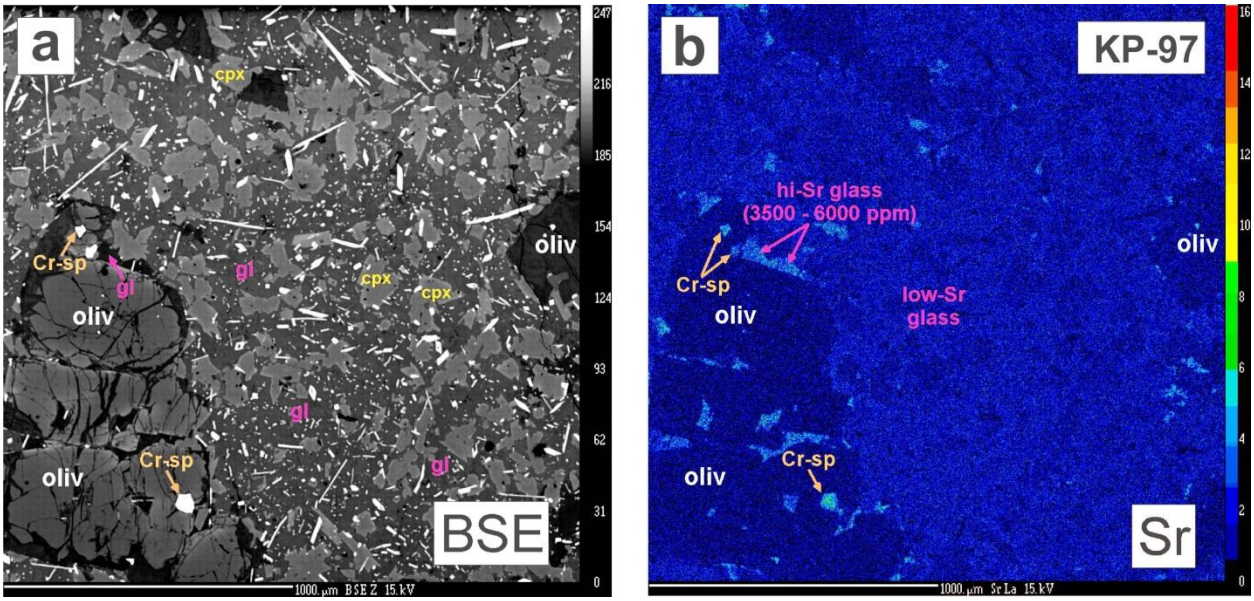


**Figure 12.** BSE (a) and X-ray map for Sr (b) in part of sample KP-97, which contains two compositionally distinct glasses. The dominant glass in the groundmass (Type 1, medium gray in BSE image) contains lower Sr (207 – 1860 ppm) relative to Type 2 glass, which occurs adjacent to olivine phenocrysts (Sr = 920 – 9470 ppm, dark gray in BSE image). Clinopyroxene grains in the groundmass show modest X-ray signals for Sr. As in Figure 11, the high apparent Sr response for Cr-rich spinel is caused by an overlap between Sr and Cr X-ray peaks.

515
516 **4.4 LA-ICPMS Analyses**
517
518 We focused our LA-ICPMS analysis on glasses and feldspars, and to a lesser extent on
519 pyroxenes in order to identify and characterize the repositories of incompatible elements in our
520 samples. Given the relatively large spot sizes (30-40 μm), compositions of glasses are quite
521 variable because of the unavoidability of incorporating variable amounts of mineral
522 contaminants, either at grain boundaries, as small inclusions or as concealed sub-glass mineral
523 grains. Mineral contaminants include olivine, clinopyroxene, ilmenite and to a lesser extent
524 apatite, whose presence is indicated by EMPA analyses for major elements. The effect of the
525 presence of these mineral contaminants on the LA-ICPMS spot analyses is to lower the
526 concentrations of incompatible elements, and so those results with the highest values of Sr, Ba,
527 Zr, REE etc. will most closely reflect the compositions of pure glasses.
528
529 LA-ICPMS results for trace elements in glasses, feldspars and clinopyroxenes are given
530 in Table S1, and are plotted for Sr, Ba and Zr in Figure 13. Plots for major and trace elements in
531 individual samples are given in Figures S4 - S9. In feldspar-free samples KP-108 and KP-142,
532 glasses least affected by mineral contamination have Sr ~3000-3400 ppm, Ba ~3000-3300 ppm,
533 Zr ~1000-1200 ppm and Ce ~400-450 ppm. For samples that contain two glass types (KP-97,
534 KP-111), the dominant groundmass glass (Type 1) has markedly lower Sr (600-1800 ppm) than
535 glass adjacent to olivine phenocrysts (Type 2), which has Sr ~2700-9500 ppm, but other
536 incompatible elements are highly variable, with no clear cut distinction between Types 1 and 2
537 (Ba ~300-5000 ppm, Zr ~200-1100 ppm, Ce ~100-400 ppm). Sample KS-35A contains both
538 glass and feldspar as groundmass phases, but the few LA-ICPMS spot analyses we obtained
539 show lower incompatible element concentrations than the whole rock values, implying that
540 additional data are needed to more accurately locate the repositories of these elements in this
541 sample. Besides glass, clinopyroxene is the only other phase that contains appreciable Sr (~130-
542 580 ppm), as measured in samples KP-97, KP-111 and KP-142 (Figure 13). A single spot
543 analysis of olivine in sample KP-111 yields very low concentrations (<5-6 ppm) for all measured
544 trace elements.

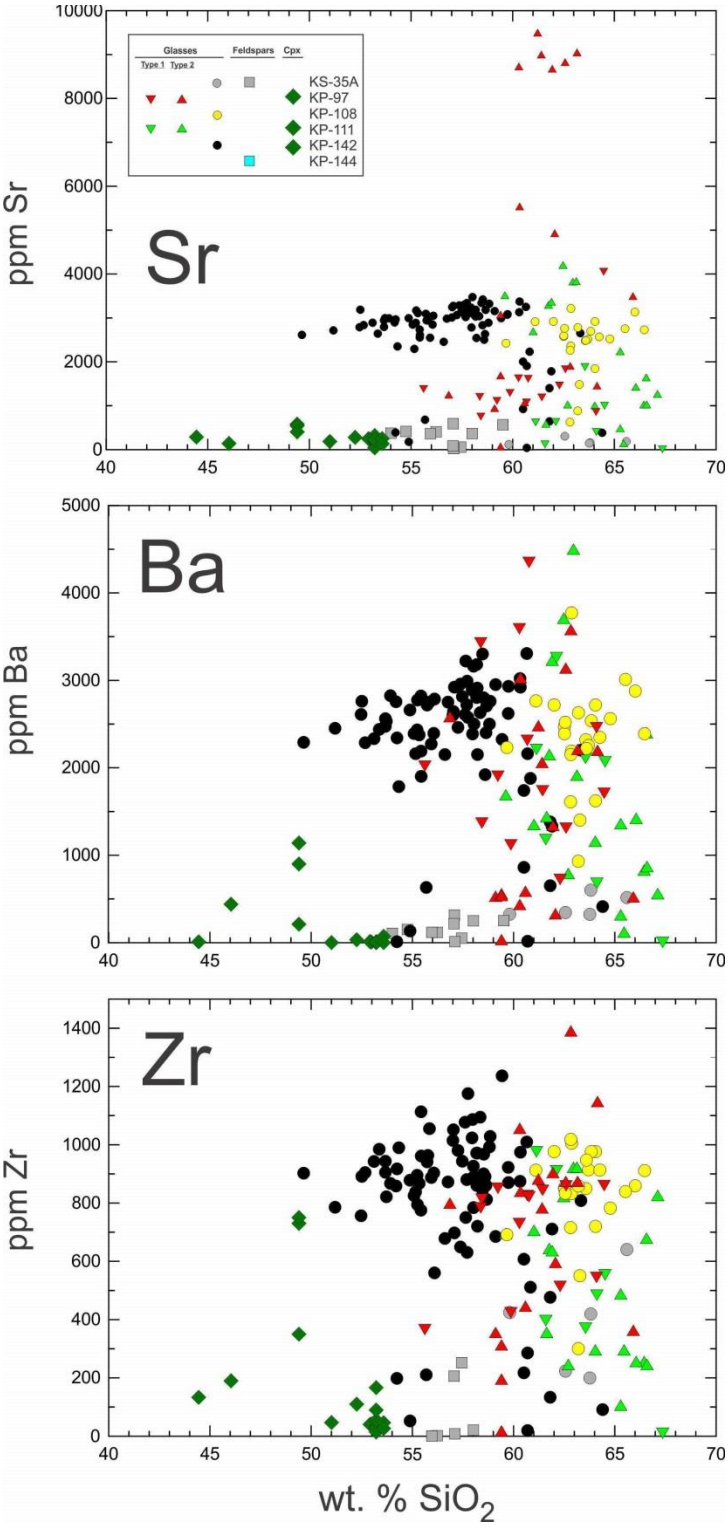


**Figure 13.** Plots of wt. % $SiO_2$ vs. Sr, Ba and Zr showing compositions of glasses in the studied picrite samples, as determined by LA-ICPMS and EPMA. Spot analyses clearly representing mixtures of glasses with incorporated mineral inclusions are omitted.

Chondrite-normalized (values from Anders and Grevesse, 1989) REE plots are shown in Figure 14. Glasses have relatively high REE abundance levels, with $La_N$ = 33-470, which in most cases are higher than their whole rock values: KP-97, $La_N$ (chondrite-normalized La concentration) = 45-307, WR = 86; KP-108, $La_N$ = 120-450, WR = 108; KP-111, $La_N$ = 95-450, WR = 160; KP-142, $La_N$ = 140-470, WR = 202. Sample KP-142, for which we have the most LA-ICPMS glass analyses (n = 98), shows this effect nicely: there is a high concentration of sub-parallel REE patterns, almost all of which plot above the whole rock pattern (Figure 14). Glass analyses with REE lower than whole rock values tend to be those affected by incorporation of mineral inclusions. Glasses are typically LREE-enriched, with $[La/Lu]_N$ ranging from ~20 to ~28; where present, Eu anomalies tend to be negative (Eu/Eu* = 0.69-0.96), although some small positive Eu anomalies with Eu/Eu* ~1.1 are also present; the majority of glass analyses show no Eu anomalies. There is near complete overlap of REE patterns for Type 1 and Type 2 glasses in samples KP-97 and KP-111. Sample KS-35A has coexisting feldspar and glass, with most feldspars showing low REE abundance levels ($La_N$ = 1.5-4.3) and prominent positive Eu anomalies (Eu/Eu* = 1.5-22.7), and most glasses showing higher total REE ($La_N$ = 30-175) and small negative Eu anomalies (Eu/Eu* = 0.63-0.74). Spot analyses of clinopyroxenes are characterized by LREE depletion, at variable abundance levels; those in KP-97 and KP-142 have $La_N$ = 3-33, whereas those in KP-111 have $La_N$ = 68-177. A single analysis of olivine in KP-111 has low REE abundances, with $La_N$ = 1.7 and $Lu_N$ = 0.14.

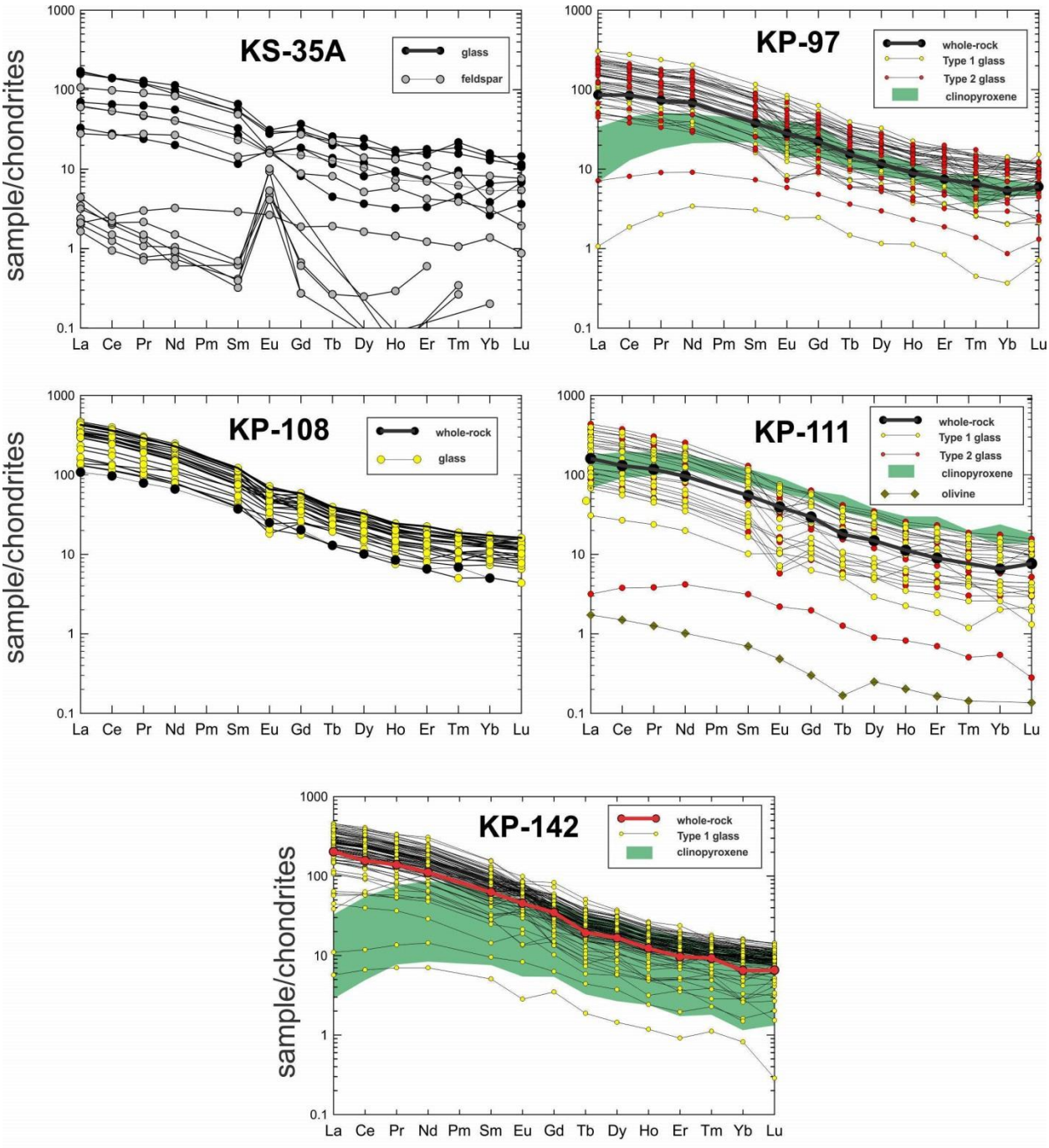


**Figure 14.** Chondrite-normalized (Anders and Grevesse, 1989) REE plots of glasses and minerals in the studied picrite samples. Obvious mixtures of glass and mineral inclusions have been omitted, but patterns for some glasses that plot below whole rock values may represent mixtures of glass and tiny mineral inclusions.

# 5 Discussion

## 5.1 Mass Balance Calculations

Based on our petrographic observations and whole rock and mineral geochemistry, the picrites we studied can be simply interpreted as two-component mixtures of variably accumulated phenocrysts and evolved residual liquids represented by bulk groundmass compositions. We computed bulk groundmass compositions for each sample by subtracting from whole rock compositions the mean phenocryst compositions given by EPMA and LA-ICPMS analyses (olivine, early Cr-rich spinel and clinopyroxene in KP-142) in their modal proportions (Table 2). Results of these calculations are given in Table S2. Whole rock compositions were normalized to 100 wt. % after recalculating FeO as 90% of $FeO_{total}$, excluding $H_2O^-$, and assuming that $H_2O^+$ or LOI represents magmatic water contained in glasses and hydrous mineral phases like apatite. Mean mineral compositions were also normalized to 100 wt. %. The calculated bulk groundmass compositions should represent the evolved residual liquids in equilibrium with the phenocrysts, and are used below to model the compositions of glasses free of contamination with mineral inclusions.

Glasses in the picrites can be assumed to represent the last phases to form in the groundmasses, after crystallization of clinopyroxene, ilmenite, late Fe-rich spinel apatite and feldspar, if present. Liquid evolution paths can be calculated by subtracting bulk groundmass minerals, in proportions given by modal abundances, from bulk groundmass compositions as determined above. Again, mean groundmass mineral compositions were normalized to 100 wt. %. In most cases, the liquid evolution trajectories for major and trace elements correspond to measured glass compositions, especially those determined to be minimally affected by mineral inclusion contamination. (Figure 15 and Figures S4 - S9). For samples with two glasses, the liquid evolution trajectories trend toward the Type 1 glass (KP-97, Figure S5) or toward a composition between Types 1 and 2 glasses (KP-111, Figure S7). These calculated liquid evolution trajectories may be compared with liquid lines of descent as determined using thermodynamically constrained fractional crystallization modelling, discussed below.

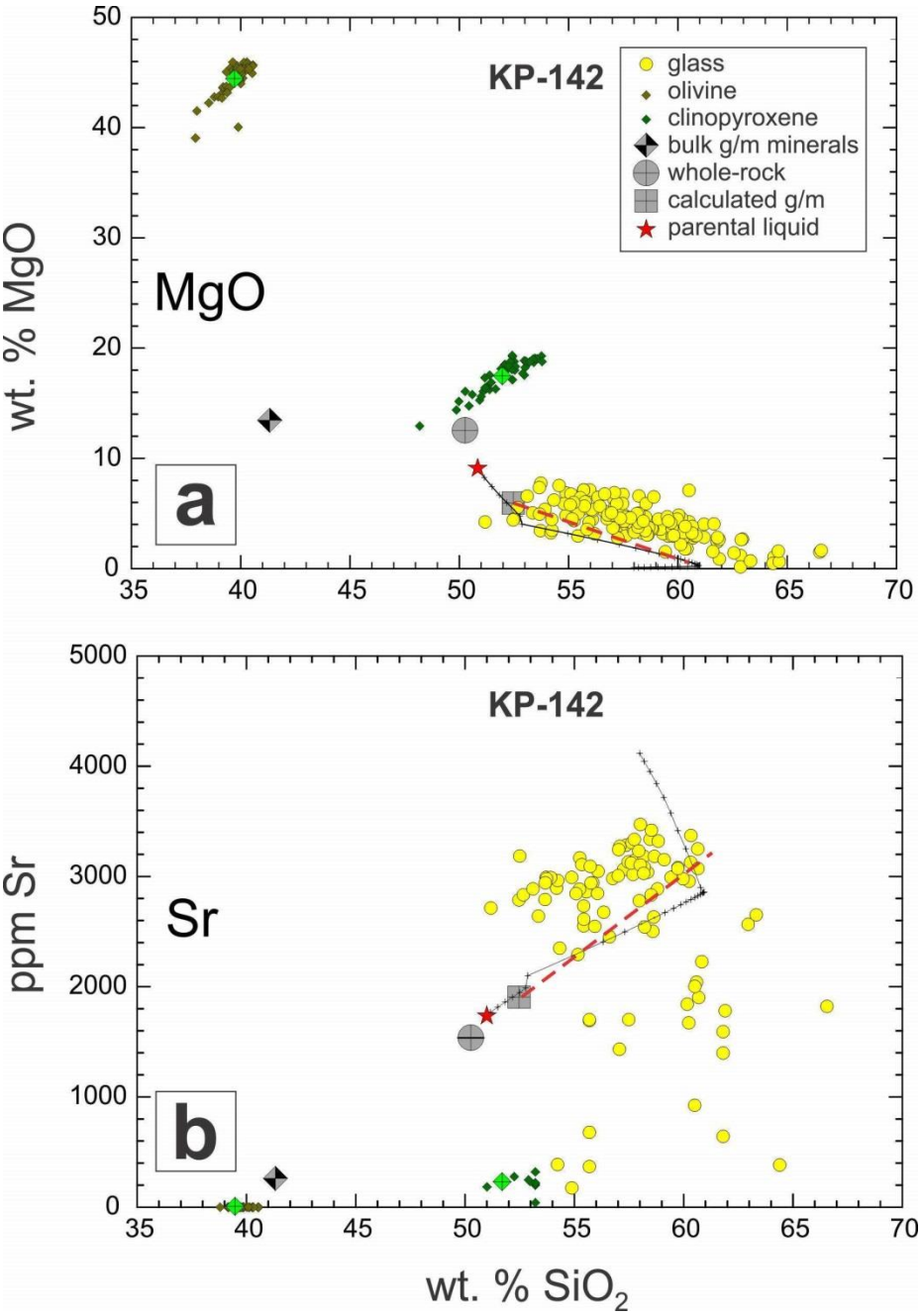


**Figure 15.** Plots of wt. % $SiO_2$ vs. MgO **(a)** and ppm Sr **(b)**, showing compositions of glasses, olivines and clinopyroxenes. Average mineral compositions are shown as large green diamonds. Also shown are compositions of whole rocks (gray crossed circles), bulk groundmass minerals calculated from modal abundances (gray crossed diamonds), bulk groundmasses calculated by subtracting bulk groundmass minerals from whole rocks (gray crossed squares), and calculated parental liquids (red stars). The results of fractional crystallization modelling using PELE are shown as black lines with + symbols at temperature intervals of 25°C. This may be compared with a simple mass balance liquid line of descent (dashed red lines) calculated by subtracting compositions of bulk groundmass minerals from that of bulk groundmasses.

Given that the picrites represent variable mixtures of accumulated phenocrysts and evolved residual liquids, the compositions of their parental melts must lie between whole rock and bulk groundmass compositions. We estimated parental liquids as mixtures of 50% each of whole rock and bulk groundmass compositions; varying these proportions makes little difference because the maximum difference between the end-members, for example in $SiO_2$, is less than about 2 wt.%. Calculations can be found in Table S2, and a summary of parental melt compositions for major and trace elements is given in Table 3. Parental melt compositions are used below for liquid evolution modelling. Average calculated parental melts have basalt-like $SiO_2$ (50.4 ± 0.6 wt. %), but lower $Al_2O_3$ (9.1 ± 0.9 wt. %) and $Na_2O$ (1.6 ± 0.8 wt. %), higher MgO (11.0 ± 1.8 wt. %), and much higher $K_2O$ (2.8 ± 1.2 wt. %) relative to the average Lesotho tholeiite (Table 3). Most trace elements, including all incompatible elements (avg. Sr = 1290 ± 329 ppm, Ba = 1217 ± 314 ppm, Zr = 493 ± 98 ppm) and even some compatible elements (avg. Ni = 520 ± 152 ppm, Cr = 551 ± 214 ppm, Co = 87 ± 25 ppm) are much higher than average Lesotho tholeiite.

## 5.2 Fractional crystallization modelling

For the Karoo picrites, we explored the details of fractional crystallization processes to account for the observed mineral and glass compositions, using the PELE (version 8.01b) modelling software (Boudreau, 1999), which is a PC platform of MELTS (Ghiorso and Sack, 1995). We used parental liquids as calculated above (Table 3) to calculate isobaric fractionation models for individual picrite samples. Input parameters were as follows: P = 5 kbar, $fO_2$ = QFM, excluded phases = orthopyroxene (absent in our samples), apatite (to suppress early crystallization of phosphate) and spinel (to prevent excessive early crystallization of Cr-rich spinel). The pressure of 5 kbar was chosen to bracket the depth of initial and final crystallization, but varying P in the range of 0-10 kbar has minimal effect on the results for liquid and solid evolution. Results are given in Table S3 and plotted for $SiO_2$ vs. MgO and Sr in sample KP-142 in Figure 15; plots for a variety of major and trace elements in individual samples are given in Figures S4 - S9. The crystallization sequences are: olivine – clinopyroxene ± Fe-rich spinel ± ilmenite – feldspar. Clinopyroxene joins olivine after about 12-30% crystallization, and late feldspar precipitates after about 50-70% crystallization, although most picrites quenched to form glass before the onset of feldspar crystallization. For most samples, the liquidus olivine compositions predicted by PELE are within a few mole % Fo of the average core olivine compositions measured by EPMA, but differ by ~6 mole % Fo for samples KP-108 and KP-144, perhaps due to underestimation of $FeO/Fe_2O_3$ in their parental liquids.

For most major and trace elements, the PELE liquid evolution models closely follow those predicted independently by the bulk groundmass and mineral calculations described above, and the calculated liquids just before feldspar crystallization best match the measured compositions of those glasses deemed to have minimal contamination by mineral phases (Figure 15; Figures S4 - S9). For feldspar-bearing samples, PELE modelled liquids either evolve to major element compositions near average measured feldspar (KP-144) or to between coexisting feldspar and glass (KS-35A); regrettably, insufficient trace element analyses have been acquired

for glasses and feldspars in these samples. In general, the correspondence of PELE models with crystallization sequences and phase composition confirms the veracity of parental liquid compositions, the origins of which are discussed below.

### 5.3 Type 1 vs. Type 2 glasses

We interpret the compositional differences between Type 2 glasses, which occur as small patches adjacent to olivine phenocrysts in samples KP-97 and KP-11, relative to the dominant (Type 1) glass in the groundmasses, as reflecting additional growth of Fe-rich olivine that occurs as thin rims along phenocryst edges. This resulted in removal of olivine components (e.g. MgO, FeO) from the Type 1 melts, and dramatic enrichment in non-olivine components ($Na_2O$ up to ~3.4 wt. %, $H_2O$ to ~13 wt. %, and Sr to ~9000 ppm) observed in the compositionally distinct Type 2 glasses (Figures 10, 13). It is difficult to evaluate this effect for other incompatible elements (e.g. Ba, Zr, REE) because of the extensive overlap for Types 1 and 2 glasses, probably caused by incorporation of mineral contaminants in the spot analyses. We are puzzled by the lack of enrichment in $K_2O$ for Type 2 glasses; no K-rich phases (e.g. K-feldspar) occur in the groundmasses of these samples. Secondary removal of K from the Type 2 glasses is a possibility, but this seems unlikely, given the absence of low-temperature secondary phases such as zeolites or clay minerals. Nevertheless, we are confident that the Type 2 glasses originated from continued magmatic precipitation of rims on olivine phenocrysts, implying *in situ* crystallization. The euhedral nature of these olivine crystals also argues against their origin as xenocrystic material blended into the picritic magmas from unrelated magmatic systems.

### 5.4 Origin of Parental Liquids

A variety of mantle and crustal sources have been proposed to account for the compositional and isotopic ranges displayed by the multiplicity of magmatic rocks in the Karoo LIP (e.g. Hawkesworth et al., 1984; Heinonen et al., 2016; Kamenetsky et al., 2017). Evaluating the role of crustal contamination in the incompatible element enrichment of mantle-derived rocks typically relies on radiogenic and stable isotope measurements, which are regrettably lacking for the picritic rocks we studied. However, on the basis of combined geochemical and isotopic data, several studies have concluded that similar Karoo enriched picrites as well as other high-Ti magmatic rocks were sourced mainly or entirely from the sub-continental mantle lithosphere (SCLM), with minimal effects of crustal contamination (e.g. Luttinen, 2018; Jourdan et al., 2007; Riley et al., 2005; Sweeney et al., 1994; Ellam and Cox, 1989; Bristow et al., 1984). In any case, our calculated parental liquids are extraordinarily enriched in incompatible trace elements (e.g. Sr = 870 – 1720 ppm, Ba = 700 – 485, Zr = 320 – 615, Table 3), with values far higher than almost all continental crustal rock types (upper continental crust, Sr = 320 ppm, Ba = 624 ppm, Zr = 193 ppm, Rudnick and Gao, 2003). Finally, Harris et al. (2015) concluded that the high $\delta^{18}O$ values of Karoo enriched picrites, similar to those studied here, could not be explained by crustal contamination, but instead requires a high $\delta^{18}O$ mantle source. We concur with those authors who conclude that the high-Ti Karoo magmatic rocks, including the alkali picrites in this study, were sourced mainly or entirely from the SCLM. Ashwal (2017) argued on the basis of

volume constraints that the enormous quantity of low-Ti Karoo tholeiites cannot have been sourced from the SCLM, but instead were generated from sub-lithospheric sources.

The bulk of the SCLM below the Kaapvaal Craton must be depleted, cold, buoyant, stable and infertile, having been formed by massive extraction of basaltic and komatiitic magmas during the early- to mid-Archean (e.g. de Wit et al., 1992; Kamber and Tomlinson, 2019). This is supported by seismic (e.g. Fouch et al., 2004) and kimberlite xenolith studies (e.g. Pearson et al., 1995; Carlson et al., 2000). If the incompatible-rich, high-Ti Karoo magmas were derived from SCLM, their sources, therefore, must be relatively small-volume enriched domains, representing either ancient subducted crustal materials (e.g. oceanic crust) or local regions metasomatized by fluids or melts. The properties of our calculated parental liquids to the picritic rocks we studied that are relevant to characterizing their mantle sources include: high MgO, $TiO_2$, $K_2O$, $P_2O_5$ and $H_2O$, low $Al_2O_3$, CaO and $Na_2O$, and very high Sr, Rb, Ba, Zr, LREE and La/Yb, relative to the average low-Ti tholeiitic basalt (Table 3). Several studies have concluded that picritic rocks similar to those studied here were derived from pyroxene-rich (pyroxenite or eclogite) rather than peridotitic sources (e.g. Heinonen and Luttinen. 2008; Harris et al., 2015; Kamenetsky et al., 2017). The high NiO (average = 0.36-0.48 wt. %), low CaO (average = 0.23-0.27 wt. %) and low MnO (average = 0.16-0.23 wt. %) of olivine phenocrysts (Table S1) also supports a non-peridotitic source (Sobolev et al., 2007; Kamenetsky et al., 2017). A garnet-bearing source, with garnet having been retained after partial melting, is supported by a variety of major and trace element ratios (Jourdan et al., 2007; Kamenetsky et al., 2017). Melting of clinopyroxene-rich sources was invoked to account for the Sr-rich alkali picrites of West Greenland by Larsen et al. (2003), citing evidence that clinopyroxenes in metasomatized mantle xenoliths may contain up to 600 ppm Sr and 200 ppm Ce. The high $K_2O$, $H_2O$, Rb and Ba in our calculated parental melts may be an indicator of pargasitic amphibole and/or phlogopite in their mantle sources, and the presence of metasomatic Ba-Ti titanites like lindsleyite ($Ba[Ti, Cr, Fe, Zr, Mg]_{21}O_{38}$) and hawthornite ($Ba[Ti, Cr, Fe, Mg]_{12}O_{19}$) (Haggerty et al., 1983) may also play a role. In any case, the nature of the alkali picrites we studied as mixtures of accumulated olivine phenocrysts and variably evolved residual melts produced by extensive fractional crystallization argues against the commonly held perception that they represent some of the most primitive of melts in the Karoo LIP (e.g. Harris et al., 2015).

Alternatively, our calculated parental liquids may themselves represent derivatives of more primitive, more mafic melts, resulting from an unknown amount of olivine fractionation. Experimental work shows that olivine fractionation from deep, near-solidus komatiitic melts, derived from a garnet lherzolite source, may produce enriched alkali picrite liquids (Milholland and Presnall, 1998). In such a scenario, the garnet lherzolite source, situated in the lower SCLM, must also be enriched in incompatible trace elements. In either case, we envisage the primitive or parental liquids that gave rise to the alkali picritic rocks we studied to have been formed by low degrees of partial melting of enriched domains in the sub-Kaapvaal SCLM. The enrichments in MgO, incompatible elements and volatile components in these rocks, their parental melts and mantle sources are suggestive of a possible link with kimberlite and carbonatite magmatism.

## 5 Conclusions

High-Ti Karoo picrites from the Letaba Formation are unusually enriched in incompatible major and trace elements, considering their high modal olivine content.

The incompatible elements reside in evolved trachytic to dacitic glasses and/or feldspars, where present. These groundmass phases are the last to form after extensive fractional crystallization of olivine, clinopyroxene, ilmenite and apatite.

Some samples contain two coexisting, compositionally distinct glasses, whose compositions correlate with textural associations. Minor volumes of glass adjacent to olivine phenocrysts have distinctly lower $K_2O$, MgO and FeO, and much higher $Na_2O$ and Sr, relative to the dominant glass phases in the groundmass. This can be attributed to removal of olivine components from resident residual melts, and implies that olivine phenocrysts are not xenocrysts, but instead formed by *in situ* crystallization.

We interpret the picrites as simple two-component mixtures of variably accumulated olivine phenocrysts with variably evolved residual liquids, represented by bulk groundmass compositions. This allows estimation of liquid lines of descent and parental melt compositions by mass balance. Calculated parental melts are enriched in MgO and $K_2O$, as well as almost all incompatible trace elements, relative to average low-Ti tholeiites that represent the vastly dominant volumes of magmas in the Karoo LIP.

Fractional crystallization modelling yields evolved residual liquids that match glass compositions, as well as trajectories corresponding to liquid evolution based on mass balance calculations involving mineral and bulk groundmass compositions.

The high-Ti, incompatible-rich Karoo picrites likely formed by small degrees of partial melting of domains within the SCLM underlying the Kaapvaal Craton that are enriched in Sr and other large ion lithophile elements. Their compositions are suggestive of a possible link between high-Ti Karoo magmas with kimberlitic and carbonatitic magmatism.

## Acknowledgments, Samples, and Data

We thank Chris Harris for providing samples and Niyko Shingange, who completed his B.Sc. Honors project relating to this subject of this paper at the University of the Witwatersrand. The LA-ICPMS facility at the University of the Witwatersrand was funded through a National Research Foundation – National Equipment Project grant (UID-105674) to RB. Critical comments by Ben Hayes on an earlier version of the manuscript were extremely helpful. This work was supported by a generous grant from the Oppenheimer Memorial Trust, and by research funds from the South African National Research Foundation. Datasets for this research are included in this paper and its supplementary information files.

## References

Anders, E. and Grevesse, N. (1989). Abundances of the elements: Meteoritic and solar. *Geochim. Cosmochim. Acta*, *53*, 197-214.

Ashwal, L.D. (2017). *Mantle sources and origin of the four overlapping continental LIPs generated throughout 2500 m.y. of Kaapvaal Craton history in southern Africa.* Abstract V34B-01, Paper presented at 2017 Fall Meeting, American Geophysical Union, New Orleans, Louisiana, 11 - 15 December, 2017.

Barnes, S.J. and Kunilov, V.Y. (2000). Spinels and Mg ilmenites from the Noril'sk 1 and Talnakh intrusions and other mafic rocks of the Siberian flood basalt province. *Econ. Geol., 95*, 1701-1717.

Barnes, S.J. and Roeder, P.L. (2001). The range of spinel compositions in terrestrial mafic and ultramafic rocks. *J. Petrol., 42*, 2279-2302.

Boudreau, A.E. (1999). PELE- a version of the MELTS software program for the PC platform. *Computers and Geosciences, 25*, 201-203.

Bristow, J.W. (1980). *The geochronology and geochemistry of Karoo volcanics in the Lebombo and adjacent areas*. Ph.D. Thesis, University of Cape Town, South Africa, 74 pp.

Bristow, J.W. (1984). Picritic rocks of the north Lebombo and south-east Zimbabwe. In A.J. Erlank (Ed.*) Petrogenesis of the Volcanic Rocks of the Karoo Province. Geological Society of South Africa Special Publication 13*, 105-123.

Bristow, J.W. and Cox, K.G. (1984). Volcanic rocks of the Lebombo-Nuanetsi-Sabi zone: classification and nomenclature. In: A.J. Erlank (Ed.) *Petrogenesis of the Volcanic Rocks of the Karoo Province. Geological Society of South Africa Special Publication 13*, 69-76.

Bristow, J.W., Allsopp, H.L., Erlank, A.J., Marsh, J.S. and Armstrong, R.A. (1984). Strontium isotope characterization of Karoo volcanic rocks. A.J. Erlank (Ed.) *Petrogenesis of the Volcanic Rocks of the Karoo Province. Geological Society of South Africa Special Publication 13*, 295-329.

Buiter, S.J.H. and Torsvik, T.H. (2014). A review of Wilson Cycle plate margins: A role for mantle plumes in continental break-up along sutures? *Gondwana Research, 26*, 627-653.

Carlson, R.W., Boyd, F.R., Shirey, S.B., Janney, P.E., Grove, T.L., Bowring, S.A., Schmitz, M.D., Dann, J.C., Bell, D.R., Gurney, J.J., Richardson, S.H., Tredoux, M., Menzies, A.H. Pearson, D.G., Hart, R.J., Wilson, A.H. and Moser, D. (2000). Continental growth, preservation and modification in southern Africa. *GSA Today, 20*, 1-7.

Cawthorn, R.G., Bristow, J.W. and Groves, D.I. (1989). Magnesian ilmenite in picritic basalts from the Karoo Province, South Africa. *Mineral. Mag., 53*, 245-252.

Cleverly, R.W. and Bristow. J.W. (1979). Revised volcanic stratigraphy of the Lebombo monocline. *South African Journal of Geology, 82*, 227-230.

Cox, K.G. (1988). The Karoo Province. In J.D. Macdougall (Ed.*) Continental Flood Basalts*, Kluwer, Dordrecht, pp. 239-271.

Cox, K.G. and Hawkesworth, C.J. (1985). Geochemical stratigraphy of the Deccan Traps at Mahabaleshwar, Western Ghats, India, with implications for open system magmatic processes. *J. Petrol., 26,* 355-377.

Cox, K.G., Johnson, R.L., Monkman, L.J., Stillman, C.J., Vail, J.R. and Wood, D.N. (1965). The geology of the Nuanetsi Igneous Province. *Philosophical Transactions of the Royal Society of London, Series A., Mathematical and Physical Sciences, 257*, 71-218.

Cox, K.G., Macdonald, R. and Horning, G. (1967). Geochemical and petrographic provinces in the Karroo basalts of southern Africa. *Amer. Mineral., 52,* 1451-1474.

de Wit, M.J., Roering, C., Hart, R.J., Armstrong, R.A., de Ronde, C.E.J., Green, R.W.E., Tredoux, M., Perbedy, E. and Hart, R.A. (1992). Formation of an Archaean continent. *Nature, 327*, 553-562.

Duncan, A.R., Erlank, A,J, and Marsh, J.S. (1984). Regional geochemistry of the Karoo igneous province. In: A.J. Erlank (Ed.) *Petrogenesis of the Volcanic Rocks of the Karoo Province. Geological Society of South Africa Special Publication 13*, 355-388.

Elkins, L.T. and Grove, T.L. (1990). Ternary feldspar experiments and thermodynamic models. *Amer. Mineral. ,75*, 544-559.

Ellam, R.M. and Cox, K.G. (1991). An interpretation of the Karoo picrite basalts in terms of interaction between asthenospheric magmas and the mantle lithosphere. *Earth Planet. Sci. Lett., 105,* 330-342.

Erlank, A.J. (Ed.) (1984). *Petrogenesis of the Volcanic Rocks of the Karoo Province. Geological Society of South Africa Special Publication 13*, 388 pp.

Ernst, R.E. (2014). Large Igneous Provinces. Cambridge University Press, 653 pp.

Ernst, R.E. and Buchan, K.L. (1997). Giant radiating dyke swarms: their use in identifying Pre-Mesozoic Large Igneous Provinces and mantle plumes. In J.J. Mahoney and M.F. Coffin (Eds.) *Large Igneous Provinces: Continental, Oceanic and Planetary Flood Volcanism. Geophysical Monograph 100*, American Geophysical Union, Washington, 297-333.

Fedorenko, V.A., Lightfoot, P.C., Naldrett, A.J., Czamansske, G.K., Hawkesworth, C.J., Wooden, J.L. and Ebel, D.S. (1996). Petrogenesis of the flood-basalt sequence at Noril'sk, north central Siberia. *International Geology Review, 38*, 99-135.

Fouch, M.J., James, D.E., VanDecar, J.C., van der Lee, S. and the Kaapvaal Seismic Group (2004). Mantle seismic structure beneath the Kaapvaal and Zimbabwe Cratons. *South African Journal of Geology, 107*, 33-44.

Ghiorso, M.S. and Sack, R.O. (1995). Chemical mass transfer in magmatic processes. IV. A revised and internally consistent thermodynamic model for the interpretation and extrapolation of liquid-solid equilibria in magmatic systems at elevated temperatures and pressures. *Contrib. Mineral. Petrol., 119*, 197-212.

Gibson, S.A., Thompson, R.N., Dickin, A.P. and Leonardos, O.H. (1995). High-Ti and low-Ti mafic potassic magmas: Key to plume-lithosphere interactions and continental flood-basalt genesis. *Earth Planet. Sci. Lett., 136*, 149-165.

Hasggerty, S.E., Smyth, J.R., Erlank, A.J., Rickard, R.S. and Danchin, R.V. (1983). Lindsleyite (Ba) and mathiasite (K): two new chromium-titanates in the chrichtonite series from the upper mantle. *Amer. Mineral., 68*, 494-505.

Harris, C., le Roux, P., Cochrane, R., Martin, L., Duncan, A.R., Marsh, J.S., le Roex, A.P. and Class, C. (2015). The oxygen isotope composition of Karoo and Etendeka picrites: high $\delta^{18}O$ mantle or crustal contamination? *Contrib. Mineral. Petrol., 170*:8, doi: 10.1007/s00410-015-1164-1

Hawkesworth, C.J., Lightfoot, P.C., Fedorenko, V.A., Blake, S., Naldrett, A.J., Doherty, W. and Gorbachev, N.S. (1995). Magma differentiation and mineralization in the Siberian continental flood basalts. *Lithos, 34*, 61-88.

Hawkesworth, C.J., Marsh, J.S., Duncan, A.R., Erlank, A.J. and Norry, M.J. (1984). The role of continental lithosphere in the generation of the Karoo volcanic rocks: evidence from combined Nd- and Sr-isotope studies. In: A.J. Erlank (Ed.) *Petrogenesis of the Volcanic Rocks of the Karoo Province. Geological Society of South Africa Special Publication 13*, 341-354.

Heinonen, J.S. and Luttinen, A.V. (2008). Jurassic dikes of Vestfjella, western Dronning MAUD Land, Antarctica: Geochemical tracing of ferropicrite sources. *Lithos,105*, 347-364.

Heinonen, J.S., Luttinen, A.V. and Bohrson, W.A. (2016). Enriched continental flood basalts from depleted mantle melts: modeling lithospheric contamination of Karoo lavas from Antarctica. *Contrib. Mineral. Petrol., 171*, https://doi.org/10.1007/s00410-015-1214-8

Jourdan, F., Bertrand, H., Schärer, U., Blichert-Toft, J., Féraud, G. and Kampunzu, A.B. (2007). Major and trace element and Sr, Nd, Hf, and Pb isotope compositions of the Karoo Large Igneous Province, Botswana-Zimbabwe: lithosphere vs mantle plume contribution. *J. Petrol., 48*, 1043-1077.

Jourdan, F., Féraud, G., Bertrand, H., Watkeys, M.K. and Renne, P.R. (2008). The $^{40}Ar/^{39}Ar$ ages of the sill complex of the Karoo large igneous province: implications for the Pliensbachian-Toarcian climate change. *Geochem. Geophys. Geosyst, 9.*

Kamber, B.S. and Tomlinson, E.L. (2019). Petrological, mineralogical and geochemical peculiarities of Archaean cratons. *Chem. Geol. 511*, 123-151.

Kamenetsky, V.S., Maas, R., Kamenetsky, M.B., Yaxley, G.M., Ehrig, K., Zellmer, G.F., Bindeman, I.N., Sobolev, A.V., Kuzman, D.V., Ivanov, A.V., Woodhead, J. and Schilling, J.-G. (2017). Multiple mantle sources of continental magmatism: Insights from "high-Ti" picrites of Karoo and other large igneous provinces. *Chemical Geology, 455*, 22-31.

Larsen, L.M., Pedersen, A.K., Sundvoll, B. and Frei, R. (2003). Alkali picrites formed by melting of old metasomatized lithospheric mantle: Manîtdlat Member, Vaigat Formation, Palaeocene of West Greenland. *J. Petrol., 44*, 3-38.

Luttinen, A.V. (2018). Bilateral geochemical asymmetry in the Karoo large igneous province. *Scientific Reports*, *8*:5223, doi: 10.1038/s41598-018-23661-3

Macdougall, J.D. (Ed.) (1988). *Continental Flood Basalts*. Kluwer, Dordrecht, 341 pp.

Mahoney, J.J. and Coffin M.F. (Eds.) (1997). *Large Igneous Provinces: Continental, Oceanic and Planetary Flood Volcanism. Geophysical Monograph 100*, American Geophysical Union, Washington, 438 pp.

Marsh, J.S., Hooper, P.R., Rehacek, J., Duncan, A., and Duncan, A.R. (1997). Stratigraphy and age of Karoo basalts of Lesotho and implications for correlations within the Karoo Igneous Province. In J.J. Mahoney and Coffin M.F. (Eds.), *Large Igneous Provinces: Continental, Oceanic and Planetary Flood Volcanism. Geophysical Monograph 100*, American Geophysical Union, Washington, pp. 247-272.

Melluso, L., Barbieri, M. and Beccaluva, L. (2004). Chemical evolution, petrogenesis, and regional chemical correlations of the flood basalt sequence in the central Deccan Traps, India. *Proc. Indian Acad. Sci. (Earth Planet. Sci.), 113*, 587-603.

Milholland, C.S. and Presnall, D.C. (1998). Liquidus phase relations in the CaO-MgO-$Al_2O_3$-$SiO_2$ system at 3.0 GPa: the aluminous pyroxene thermal divide and high-pressure fractionation of picritic and komatiitic magmas. *J. Petrol., 39*, 3-27.

Natali, C., Beccaluva, L., Bianchini, G. and Siena. F. (2017). Comparison among Ethiopia-Yemen, Deccan, and Karoo continental flood basalts of central Gondwana: Insights on lithosphere versus asthenosphere contributions in compositionally zoned magmatic provinces. In G. Bianchini, K.-L. Bodiner, R. Braga and M. Wilson (Eds.) *The Crust-Mantle and Lithosphere-Asthenosphere Boundaries: Insights from Xenoliths, Orogenic Deep Sections, and Geophysical Studies. Geol. Soc. Amer Sp. Paper 526*, doi: 10.1130/2017.2526(10)

Paton, C., Woodhead, J. D., Hellstrom, J. C., Hergt, J. M., Greig, A. and Maas, R. (2010). Improved laser ablation U-Pb zircon geochronology through robust downhole fractionation correction. *Geochem. Geophys. Geosyst*, 11(3).

Paton, C., Hellstrom, J., Paul, B., Woodhead, J., & Hergt, J. (2011). Iolite: Freeware for the visualisation and processing of mass spectrometric data. *Journal of Analytical Atomic Spectrometry, 26(12*), 2508-2518.

Pearson, D.G., Carlson R.W., Shirey, S.B., Boyd, F.R. and Nixon, P.H. (1995). Stabilisation of Archaean lithospheric mantle: a Re-Os isotope study of peridotite xenoliths from the Kaapvaal Craton. *Earth Planet. Sci. Lett., 134*, 341-357.

Peate, D.W., Hawkesworth, C.J. and Mantovani, M.S.M. (1992). Chemical stratigraphy of the Parana lavas (South America): Classification of magma types and their spatial distribution. *Bull. Volcanol., 55*, 119-139.

Rudnick, R.L. and Gao, S. (2003). Composition of the continental crust. *Treatise on Geochemistry, 3*, 1-64.

Scowen, P.A.H., Roeder, P.L. and Helz, R.T. (1991). Reequilibration of chromite within Kilauea Iki lava lake, Hawaii. *Contrib. Mineral. Petrol., 107*, 8-20.

Sobolev, A.V., Hofmann, A.W., Kuzmin, D.V., Yaxley, G.M., Arndt, N.T., Chung, S.-L., Danyushevsky, L.V., Elliott, T., Frey, F.A., Garcia, M.O., Gurenko, A.A., Kamenetsky, V.S., Kerr, A.C., Krivolutskaya, N.A., Matvienkov, V.V., Nikogosian, I.K., Rocholl, A., Sigurdsson, I.A., Sushchevskaya, N.M., Teklay, M. (2007). The amount of recycled crust in sources of mantle-derived melts. *Science, 316*, 412–417.

Storey, B.C. (1995). The role of mantle plumes in continental breakup: case histories from Gondwanaland. *Nature, 377*, 301-308.

Storey, B.C. and Kyle, P.R. (1997). An active mantle mechanism for Gondwana breakup. *South African Journal of Geology, 100*, 283-290.

Svensen, H., Corfu, F., Polteau, S., Hammer, Ø. And Planke, S. (2012). Rapid magma emplacement in the Karoo Large Igneous Province. *Earth Planet. Sci. Lett., 325-326*, 1-9.

Sweeney, R.J., Duncan, A.R. and Erlank, A.J. (1994). Geochemistry and petrogenesis of Central Lembombo basalts from the Karoo Igneous Province. *J. Petrol., 35*, 95-125.

Wyatt, B.A., Baumgartner, M., Anckar, E. and Grutter, H.S. (2004). Compositional classification of "kimberlitic" and "non-kimberlitic" ilmenite. *Lithos, 77*, 819-840.

**Table 1. Whole rock major and trace element compositions of Karoo picrites**

| | KS-35a | KP-97 | | KP-108 | | KP-111 | | KP-142 | | KP-144 | | Average Karoo picrite | |
|---|---|---|---|---|---|---|---|---|---|---|---|---|---|
| **Data Source[1]** | 1 | 1 | 2 | 1 | 2 | 1 | 2 | 1 | 2 | 1 | 2 | **n = 897** | |
| **Latitude** | -23.1686 | -22.6111 | | -22.4944 | | -22.4819 | | -22.3511 | | -22.3817 | | | std |
| **Longitude** | 31.5053 | 31.2222 | | 31.2014 | | 31.2192 | | 31.1247 | | 31.2142 | | avg | dev |
| **$SiO_2$** | 49.96 | 48.65 | 46.59 | 47.20 | 45.70 | 49.26 | 47.24 | 50.27 | 49.84 | 49.16 | 49.48 | 48.42 | 1.71 |
| **$TiO_2$** | 2.68 | 3.19 | 2.73 | 2.51 | 2.16 | 3.17 | 2.97 | 3.84 | 3.39 | 3.17 | 2.87 | 2.33 | 0.82 |
| **$Al_2O_3$** | 9.95 | 7.01 | 6.00 | 6.54 | 5.61 | 8.00 | 7.28 | 8.46 | 7.50 | 8.10 | 7.29 | 9.04 | 1.79 |
| ***FeO*** $^T$ | | | *11.73* | | *11.13* | | *10.31* | | *10.80* | | *11.13* | | |
| ***$Fe_2O_3$*** $^T$ | *12.52* | *11.59* | | *11.59* | | *10.60* | | *10.99* | | *10.60* | | | |
| **FeO[2]** | 10.14 | 9.39 | 10.55 | 9.39 | 10.02 | 8.58 | 9.27 | 8.90 | 9.72 | 8.58 | 10.02 | 9.38 | 0.91 |
| **$Fe_2O_3$** [2] | 1.25 | 1.16 | 1.30 | 1.16 | 1.24 | 1.06 | 1.15 | 1.10 | 1.20 | 1.06 | 1.24 | 1.84 | 0.18 |
| **MnO** | 0.17 | 0.14 | 0.15 | 0.14 | 0.15 | 0.14 | 0.14 | 0.14 | 0.14 | 0.13 | 0.15 | 0.16 | 0.03 |
| **MgO** | 11.30 | 16.44 | 20.72 | 20.52 | 24.17 | 13.92 | 15.75 | 12.53 | 14.45 | 14.53 | 18.17 | 15.39 | 3.24 |
| **CaO** | 8.63 | 6.22 | 5.10 | 5.62 | 4.57 | 6.71 | 5.99 | 7.00 | 6.01 | 6.40 | 5.46 | 7.43 | 1.33 |
| **$Na_2O$** | 1.92 | 0.27 | 0.27 | 1.98 | 1.55 | 1.51 | 1.47 | 1.16 | 1.09 | 1.31 | 1.16 | 1.46 | 0.47 |
| **$K_2O$** | 1.67 | 4.02 | 3.14 | 0.97 | 0.79 | 2.47 | 2.02 | 3.05 | 2.55 | 2.69 | 2.28 | 1.30 | 0.86 |
| **$P_2O_5$** | 0.40 | 0.53 | 0.45 | 0.46 | 0.37 | 0.55 | 0.52 | 0.57 | 0.51 | 0.48 | 0.42 | 0.35 | 0.15 |
| **$H_2O^+$** | 1.77 | 1.91 | n.d. | 3.29 | n.d. | 3.14 | n.d. | 3.22 | n.d. | 2.12 | n.d. | 0.00 | |
| **$H_2O$-** | 0.39 | 0.45 | n.d. | 0.33 | n.d. | 0.81 | n.d. | 0.55 | n.d. | 0.55 | n.d. | 0.00 | |
| **LOI** | 2.16[3] | 2.36[3] | 2.99[4] | 3.62[3] | 3.67[4] | 3.95[3] | 6.20[4] | 3.77[3] | 3.60[4] | 2.67[3] | 1.46[4] | 2.91 | 1.42 |
| **Total** | 100.23 | 99.38 | 100.00 | 100.11 | 100.00 | 99.32 | 100.00 | 100.79 | 100.00 | 98.28 | 100.00 | 100.00 | |
| **mg#[5]** | 66.51 | 75.73 | 77.77 | 79.57 | 81.13 | 74.30 | 75.16 | 71.50 | 72.60 | 75.11 | 76.37 | 74.04 | 3.90 |
| **$Na_2O + K_2O$** | 3.59 | 4.29 | 3.41 | 2.95 | 2.34 | 3.98 | 3.49 | 4.21 | 3.64 | 4.00 | 3.44 | 2.84 | 0.91 |
| **ppm** | | | | | | | | | | | | | |
| **Cs** | | | 0.51 | | 0.69 | | 2.34 | | 1.12 | | 0.74 | 0.95 | 0.76 |
| **Rb** | 36 | 82 | 67.7 | 67 | 52.3 | 101 | 85.6 | 56 | 46.7 | 53 | 45 | 29.92 | 19.81 |
| **Ba** | 667 | 840 | 665 | 1076 | 841 | 1154 | 1110 | 1295 | 1194 | 1320 | 1096 | 603.86 | 373.98 |
| **Th** | | | 3.5 | | 4.07 | | 6.07 | | 5.58 | | 6.23 | 3.86 | 2.10 |
| **U** | | | 0.34 | | 0.9 | | 1.23 | | 1.01 | | 1.27 | 2.41 | 2.34 |
| **Nb** | | 19.8 | 18.73 | 21.9 | 18.92 | 27.1 | 24.34 | 27.9 | 14.83 | 34 | 21.77 | 17.55 | 9.25 |
| **Ta** | | | 1.3 | | 1.7 | | 2.3 | | 2.4 | | 2.6 | 0.92 | 0.80 |
| **La** | | | 38.4 | | 48.1 | | 71.4 | | 90.2 | | 69.3 | 35.34 | 20.68 |
| **Ce** | | | 95.7 | | 109.9 | | 148.1 | | 177.5 | | 154.4 | 77.46 | 44.89 |
| **Pb** | | | n.d. | | n.d. | | *8* | | *8* | | *7* | 5.49 | 4.69 |
| **Pr** | | | 12.25 | | 13.15 | | 19.54 | | 23.12 | | 18.78 | 9.25 | 6.66 |
| **Sr** | 826 | 870 | 820 | 956 | 834 | 1168 | 1102 | 1536 | 1304 | 1417 | 1220 | 697.19 | 345.34 |
| **Nd** | | | 56.4 | | 54.8 | | 79.5 | | 91.8 | | 75.1 | 47.37 | 24.86 |
| **Sm** | | | 9.78 | | 9.59 | | 14.2 | | 16.23 | | 12.5 | 7.75 | 4.57 |
| **Zr** | 302 | 415 | 307 | 390 | 281 | 451 | 404 | 547 | 453 | 474 | 385 | 266.53 | 130.75 |
| **Hf** | | | 7.9 | | 7.4 | | 10.8 | | 12.1 | | 9.8 | 5.27 | 3.80 |
| **Eu** | | | 2.73 | | 2.43 | | 3.84 | | 4.42 | | 3.27 | 2.31 | 1.15 |
| **Gd** | | | 7.36 | | 6.69 | | 9.71 | | 11.43 | | 8.79 | 6.62 | 3.16 |
| **Tb** | | | 0.93 | | 0.78 | | 1.08 | | 1.16 | | 1.02 | 0.96 | 0.35 |
| **Dy** | | | 4.59 | | 3.97 | | 5.84 | | 6.56 | | 5.07 | 5.23 | 1.64 |
| **Y** | 29.4 | 26.5 | 19.4 | 22.6 | 15.6 | 27 | 24.1 | 31.6 | 26 | 27.5 | 21 | 25.10 | 5.60 |
| **Ho** | | | 0.79 | | 0.75 | | 1 | | 1.1 | | 0.83 | 0.93 | 0.31 |
| **Er** | | | 1.87 | | 1.64 | | 2.24 | | 2.42 | | 2.00 | 2.24 | 0.67 |
| **Tm** | | | 0.25 | | 0.26 | | 0.34 | | 0.35 | | 0.29 | 0.39 | 0.42 |
| **Yb** | | | 1.32 | | 1.24 | | 1.62 | | 1.6 | | 1.47 | 1.73 | 0.97 |
| **Lu** | | | 0.22 | | 0.19 | | 0.28 | | 0.24 | | 0.22 | 0.23 | 0.07 |
| **Be** | | | 1.5 | | 1.3 | | 1.7 | | 1.8 | | 1.8 | | |
| **Sc** | 26.6 | 21 | 16.4 | 16.3 | 14.6 | 20.1 | 18.6 | 22.5 | 19.3 | 18.9 | 16.5 | 21.39 | 4.98 |
| **V** | 246 | 200 | 186 | 155 | 152 | 201 | 208 | 215 | 219 | 180 | 173 | 214.66 | 113.74 |

| | | | | | | | | | | | | | |
|---|---|---|---|---|---|---|---|---|---|---|---|---|---|
| **Cr** | 636 | 858 | 932 | 861 | 824 | 792 | 862 | 699 | 949 | 700 | 826 | 912.88 | 305.36 |
| **Co** | 69 | 77 | 88.8 | 105 | 95.4 | 66 | 65.8 | 64 | 71.2 | 70 | 78.7 | 75.40 | 13.34 |
| **Ni** | 495 | 920 | 1179 | 1306 | 1491 | 709 | 816 | 618 | 737 | 779 | 936 | 723.37 | 252.06 |
| **Cu** | 88 | 84 | 76 | 74 | 83 | 91 | 100 | 93 | 98 | 84 | 81 | 79.61 | 22.50 |
| **Zn** | 110 | 110 | 124 | 106 | 106 | 99 | 98 | 109 | 105 | 99 | 101 | 105.43 | 12.44 |
| **Mo** | | | 1 | | 1.1 | | 1.1 | | 0.8 | | 1.2 | 1.54 | 1.15 |
| **Ga** | | | 12.3 | | 11.7 | | 16.1 | | 16.5 | | 13.7 | 14.50 | 3.74 |
| **Sn** | | | 4 | | 4 | | 5 | | 5 | | 4 | 4.30 | 1.53 |
| **Li** | | | 5 | | 10 | | 14 | | 9 | | 10 | | 0.03 |

**[1]Data Sources:**

1. **Bristow (1980); Bristow et al. (1984)**
2. **Kamenetsky et al. (2017)**

**[2]Calculated with FeO = 90% $FeO^{T}$**

**[3]$H_2O^+ + H_2O^-$**

**[4]Calculated by difference from 100%**

**[5]$100Mg/(Mg+Fe^{2+})$**

**Table 2. Petrographically estimated modal abundances of Karoo picrites**

| | KS-35A | KP-97 | KP-108 | KP-111 | KP-142 | KP-144 |
|---|---|---|---|---|---|---|
| Phenocrysts (%) | 10 | 23 | 37 | 20 | 20 | 20 |
| Olivine | 94 | 82 | 90 | 89.1 | 64.2 | 89.1 |
| Altered Olivine | 5 | 17.5 | 9 | 9.9 | 15.8 | 9.9 |
| Clinopyroxene | | | | | 19 | |
| Cr-rich spinel | 1 | 0.5 | 1 | 1 | 1 | 1 |
| | 100 | 100 | 100 | 100 | 100 | 100 |
| Groundmass (%) | 90 | 77 | 63 | 80 | 80 | 80 |
| Glass, Type 1 | 35 | 48.2 | | 33.1 | 55 | |
| Glass, Type 2 | | 5.3 | 56.4 | 17.9 | | |
| Feldspar | 39 | | | | | 49 |
| Clinopyroxene | 20 | 36.7 | 34.4 | 39.2 | 33.3 | 40 |
| Ilmenite | 5 | 5.6 | 3.9 | 4.4 | 8.5 | 10 |
| Mt-rich spinel | | 3.3 | 4.4 | 4.4 | 1.8 | |
| Apatite | 1 | 0.9 | 0.9 | 1 | 1.4 | 1 |
| | 100 | 100 | 100 | 100 | 100 | 100 |
| OVERALL MODE | | | | | | |
| Olivine | 9.4 | 18.9 | 33.3 | 17.8 | 12.8 | 17.8 |
| Altered Olivine | 0.5 | 4.0 | 3.3 | 2.0 | 3.2 | 2.0 |
| Glass, Type 1 | 31.5 | 37.1 | | 26.5 | 44.0 | 0.0 |
| Glass, Type 2 | | 4.1 | 35.5 | 14.3 | | |
| Feldspar | 35.1 | 0.0 | 0.0 | 0.0 | 0.0 | 39.2 |
| Clinopyroxene | 18 | 28.3 | 21.7 | 31.4 | 32.6 | 32.0 |
| Ilmenite | 4.5 | 4.3 | 2.5 | 3.5 | 5.0 | 8.0 |
| Mt-rich spinel | | 2.5 | 2.8 | 3.5 | 1.1 | |
| Cr-rich spinel | 0.1 | 0.1 | 0.4 | 0.2 | 0.2 | 0.2 |
| Apatite | 0.9 | 0.7 | 0.6 | 0.8 | 1.1 | 0.8 |
| | 100 | 100 | 100 | 100 | 100 | 100 |
| Mean olivine core Fo | 83.8 ± 2.1 | 83.8 ± 1.0 | 84.5 ± 3.6 | 87.1 ± 2.3 | 83.3 ± 0.5 | 82.0 ± 1.1 |
| number of analyses | 20 | 25 | 21 | 24 | 47 | 9 |
| Olivine rims | | | | | | |
| Min Fo | 65.1 | 72.0 | 65.8 | 61.9 | serp* | 77.7 |
| Max Fo | 79.5 | 81.9 | 82.5 | 86.4 | serp* | 79.3 |
| number of analyses | 22 | 10 | 15 | 17 | | 4 |

serp* rims obliterated by serpentine alteration

**Table 3. Calculated parental liquids for Karoo picrites**

| | | | | | | | Average calculated parental liquid n = 6 | | | Average Lesotho tholeiite n = 579 | |
|---|---|---|---|---|---|---|---|---|---|---|---|
| | KS-35A | KP-97 | KP-108 | KP-111 | KP-142 | KP-144 | avg | std dev | Range | avg | std dev |
| $SiO_2$ | 50.51 | 50.18 | 49.29 | 50.76 | 50.84 | 50.83 | **50.40** | 0.60 | 49 - 51 | **50.19** | 0.91 |
| $TiO_2$ | 2.83 | 3.68 | 3.21 | 3.58 | 4.24 | 3.60 | **3.52** | 0.47 | 2.8 - 4.2 | **1.00** | 0.13 |
| $Al_2O_3$ | 10.50 | 8.09 | 8.37 | 9.03 | 9.38 | 9.17 | **9.09** | 0.85 | 8 - 10.5 | **14.95** | 0.77 |
| $Cr_2O_3$ | 0.09 | 0.10 | 0.00 | 0.06 | 0.04 | 0.11 | **0.07** | 0.04 | | | |
| FeO | 9.89 | 8.59 | 7.82 | 8.16 | 8.17 | 7.71 | **8.39** | 0.79 | 7.8 - 9.9 | **8.63** | 0.81 |
| $Fe_2O_3$ | 1.32 | 1.33 | 1.48 | 1.19 | 1.22 | 1.21 | **1.29** | 0.11 | 1.2 - 1.5 | **1.69** | 0.16 |
| MnO | 0.17 | 0.13 | 0.12 | 0.14 | 0.13 | 0.12 | **0.13** | 0.02 | 0.12 - 0.17 | **0.18** | 0.02 |
| MgO | 9.52 | 12.45 | 13.54 | 9.94 | 9.13 | 11.29 | **10.98** | 1.76 | 9 - 13.5 | **6.86** | 1.24 |
| CaO | 9.09 | 7.15 | 7.16 | 7.56 | 7.33 | 7.25 | **7.59** | 0.75 | 7 - 9 | **10.33** | 0.70 |
| $Na_2O$ | 2.02 | 0.31 | 2.53 | 1.70 | 1.29 | 1.49 | **1.56** | 0.75 | 1.5 - 2.5 | **2.13** | 0.36 |
| $K_2O$ | 1.76 | 4.64 | 1.25 | 2.79 | 3.39 | 3.06 | **2.82** | 1.21 | 1.3 - 4.6 | **0.67** | 0.35 |
| $P_2O_5$ | 0.42 | 0.61 | 0.58 | 0.62 | 0.63 | 0.55 | **0.57** | 0.08 | 0.4 - 0.6 | **0.17** | 0.03 |
| $H_2O^+$ | 1.86 | 2.73 | 4.66 | 4.47 | 4.20 | 3.62 | **3.59** | 1.10 | 1.9 - 4.7 | | |
| $H_2O$- | | | | | | | | | | | |
| LOI | | | | | | | | | | **3.19** | 1.41 |
| Total | 100.00 | 100.00 | 100.00 | 100.00 | 100.00 | 100.00 | **100.00** | | | **100.00** | |
| Mg# | 63.19 | 72.10 | 75.51 | 68.46 | 64.82 | 72.28 | **69.39** | 4.76 | 63 - 75 | **58.37** | 4.49 |
| $Na_2O + K_2O$ | 3.79 | 4.95 | 3.77 | 4.50 | 4.68 | 4.55 | **4.37** | 0.49 | 3.8 - 5 | **2.88** | 0.64 |
| ppm | | | | | | | | | | | |
| Nb | | 36.27 | 28.33 | 30.49 | 31.39 | 38.25 | **32.95** | 4.15 | 28 - 30 | **7.19** | 2.89 |
| Zr | 318.78 | 476.98 | 504.52 | 507.38 | 615.38 | 533.25 | **492.71** | 97.51 | 320 - 615 | **96.85** | 17.78 |
| Y | 31.03 | 30.46 | 29.24 | 30.38 | 35.55 | 30.94 | **31.27** | 2.19 | 29 - 35 | **26.70** | 3.85 |
| Sr | 871.89 | 999.94 | 1236.73 | 1314.00 | 1720.88 | 1594.13 | **1289.59** | 328.79 | 870 - 1720 | **191.25** | 42.21 |
| Rb | 38.00 | 94.25 | 86.67 | 113.63 | 63.00 | 59.63 | **75.86** | 27.36 | 60 - 114 | **14.51** | 17.22 |
| Zn | 116.11 | 93.32 | 56.70 | 84.53 | 98.18 | 111.36 | **93.37** | 21.38 | 56 - 116 | | |
| Cu | 92.89 | 96.55 | 95.73 | 102.38 | 104.63 | 94.50 | **97.78** | 4.66 | 93 - 105 | **98.82** | 23.92 |
| Ni | 522.50 | 573.79 | 784.78 | 358.63 | 398.69 | 479.63 | **519.67** | 151.92 | 360 - 785 | **84.50** | 43.76 |
| Co | 72.83 | 88.50 | 135.83 | 74.25 | 72.00 | 78.75 | **87.03** | 24.67 | 72 - 135 | **44.73** | 5.77 |
| Cr | 671.33 | 683.27 | | 340.15 | 299.79 | 759.25 | **550.76** | 213.84 | 300 - 760 | **254.26** | 104.53 |
| V | 259.67 | 229.87 | 200.52 | 226.13 | 241.88 | 202.50 | **226.76** | 22.80 | 200 - 260 | **252.84** | 31.04 |
| Ba | 704.06 | 965.45 | 1391.97 | 1298.25 | 1456.88 | 1485.00 | **1216.93** | 314.00 | 700 - 1485 | **206.72** | 53.23 |
| Sc | 27.02 | 24.14 | 21.09 | 22.61 | 25.31 | 21.26 | **23.57** | 2.35 | 21 - 27 | **33.72** | 3.74 |
| La | | 44.14 | 62.22 | 80.33 | 101.48 | 77.96 | **73.22** | 21.44 | 44 - 101 | **11.68** | 3.06 |
| Ce | | 109.99 | 142.17 | 166.61 | 199.69 | 173.70 | **158.43** | 33.96 | 142 - 200 | **26.89** | 4.80 |
| Pr | | 14.08 | 17.01 | 21.98 | 26.01 | 21.13 | **20.04** | 4.62 | 14 - 26 | | |
| Nd | | 64.82 | 70.89 | 89.44 | 103.28 | 84.49 | **82.58** | 15.25 | 65 - 103 | **14.62** | 8.04 |
| Sm | | 11.241 | 12.406 | 15.975 | 18.259 | 14.063 | **14.39** | 2.80 | 11 - 18 | **3.86** | 0.77 |
| Eu | | 3.138 | 3.144 | 4.320 | 4.973 | 3.679 | **3.85** | 0.79 | 3 - 5 | | |
| Gd | | 8.459 | 8.655 | 10.924 | 12.859 | 9.889 | **10.16** | 1.81 | 8 - 13 | **23.33** | 7.09 |
| Tb | | 1.069 | 1.009 | 1.215 | 1.305 | 1.148 | **1.15** | 0.12 | 1.1 - 1.3 | **3.77** | 1.58 |
| Dy | | 5.276 | 5.136 | 6.570 | 7.380 | 5.704 | **6.01** | 0.95 | 5 - 7 | **18.10** | 11.76 |
| Ho | | 0.908 | 0.970 | 1.125 | 1.238 | 0.934 | **1.03** | 0.14 | 0.9 - 1.2 | **3.36** | 2.36 |
| Er | | 2.149 | 2.122 | 2.520 | 2.723 | 2.250 | **2.35** | 0.26 | 2.1 - 2.7 | **6.29** | 2.81 |
| Tm | | 0.287 | 0.336 | | 0.394 | 0.326 | **0.34** | 0.04 | 0.28 - | **0.81** | 0.34 |

| | | | | | | | | | | | |
|---|---|---|---|---|---|---|---|---|---|---|---|
| **Yb** | | 1.517 | 1.604 | 1.823 | 1.800 | 1.654 | **1.68** | 0.13 | 0.40<br>1.5 - 1.8 | **5.45** | 3.39 |
| **Lu** | | 0.253 | | 0.315 | 0.270 | 0.248 | **0.27** | 0.03 | 0.25 -<br>0.32 | **0.52** | 0.10 |
| **CIPW Weight Norm** | | | | | | | | | | | |
| **quartz** | | | | 1.79 | 3.55 | 0.45 | **0.09** | | | **2.55** | |
| **plagioclase** | 31.68 | 9.46 | 29.92 | 23.57 | 20.89 | 22.04 | **22.91** | | | **48.47** | |
| **orthoclase** | 11.16 | 28.87 | 8.84 | 18.29 | 22.04 | 19.85 | **18.21** | | | **4.22** | |
| **diopside** | 23.50 | 20.63 | 20.62 | 21.39 | 19.63 | 19.89 | **20.96** | | | **14.96** | |
| **hypersthene** | 23.34 | 27.93 | 21.51 | 24.32 | 21.78 | 27.33 | **27.32** | | | **23.65** | |
| **olivine** | 1.66 | 2.20 | 8.92 | | | | | | | | |
| **ilmenite** | 5.47 | 7.16 | 6.36 | 7.08 | 8.36 | 7.07 | **6.89** | | | **1.96** | |
| **magnetite** | 1.94 | 1.97 | 2.23 | 1.80 | 1.84 | 1.81 | **1.93** | | | **2.51** | |
| **apatite** | 1.00 | 1.44 | 1.41 | 1.51 | 1.51 | 1.32 | **1.37** | | | **1.6** | |
| **zircon** | 0.06 | 0.10 | 0.10 | 0.10 | 0.13 | 0.10 | **0.10** | | | **0.01** | |
| **chromite** | 0.15 | 0.15 | 0.00 | 0.07 | 0.07 | 0.04 | **0.12** | | | **0.06** | |
| | 99.96 | 99.91 | 99.91 | 99.92 | 99.80 | 99.90 | **99.90** | | | **99.99** | |